Nanoscale

PAPER

View Article Online
View Journal | View Issue

Cite this: *Nanoscale*, 2025, **17**, 5838

Surface-engineered core–shell upconversion nanoparticles for effective hypericin delivery and multimodal imaging†

Taras Vasylyshyn,[a] Veronika Huntošová, *[b,c] Vitalii Patsula,[a] Sona Olejárová,[d] Cyril Slabý,[d] Zuzana Jurašeková,[d] Gregor Bánó,[d] Jana Kubacková,[e] Miroslav Šlouf,[a] Oleksandr Shapoval[a] and Daniel Horák *[a]

Early diagnosis and treatment of cancer is rapidly advancing thanks to the development of nanotechnology. Here, upconversion nanoparticles (UCNPs) are particularly promising as they are finding a wide range of applications in drug delivery and tumor imaging. In this report, a novel UCNP-based transport system is proposed for the delivery of the hypericin (Hyp) photosensitizer into malignant tumors. Core–shell $NaYF_4$:Yb^{3+},Er^{3+}@$NaYF_4$:Nd^{3+} UCNPs were prepared by thermal decomposition and coated with poly(*N*,*N*-dimethylacrylamide-*co*-2-aminoethyl acrylate)-alendronate [P(DMA-AEA)-Ale], which endowed them with colloidal and chemical stability; finally, Hyp was conjugated. Internalization of CS-UCNP@P(DMA-AEA)-Ale-Hyp nanoparticles by Jurkat cells was successfully validated by multimodal imaging using a microstructural chamber, upconversion luminescence, and Raman microspectroscopy. After irradiation at 590 nm, CS-UCNP@P(DMA-AEA)-Ale-Hyp nanoparticles provided a markedly more effective photodynamic effect than Hyp alone at identical Hyp concentrations due to apoptosis as confirmed by caspase-3 activation. MTT assays showed that Hyp-free nanoparticles were non-cytotoxic, whereas CS-UCNP@P(DMA-AEA)-Ale-Hyp particles significantly reduced cell viability after irradiation. Considering that Hyp release from the nanoparticles was higher in the acidic environment typical of tumors compared to physiological ones, UCNP@P(DMA-AEA)-Ale-Hyp particles are a suitable candidate for future *in vivo* applications.

Received 19th December 2024,
Accepted 17th January 2025

DOI: 10.1039/d4nr05348f

rsc.li/nanoscale

1. Introduction

Biomedical applications of nanomaterials, such as bioimaging, optogenetics or photodynamic therapy (PDT), are nowadays in the focus of the scientific community because they are effective for patient-friendly treatments.[1–3] Compared to conventional cancer treatments such as chemotherapy and radiotherapy, PDT is a non-invasive, localized method with a significantly lower impact on surrounding healthy tissues. PDT is currently used clinically for a variety of early-stage cancers,[4] including esophageal,[5] oral[6] and lung[7] cancers, skin metastases,[8] *etc*. The active component of PDT is a photosensitizer (PS), which is excited by incident light and after interacting with surrounding molecules produces reactive oxygen species (ROS) that cause cancer cell death.[9,10] Recently, various PSs have been proposed for PDT, such as chlorin e6, verteporfin, temoporfin,[11] Rose Bengal,[12] hypericin (Hyp),[13] *etc*. The latter is a natural compound extracted mainly from St John's wort, which has excellent photosensitivity, antitumor and antiviral activity, and low toxicity.[14,15] The main disadvantages of free Hyp are hydrophobicity, which reduces its ability to generate ROS in aqueous environments due to aggregate formation, and specific resistance in tumors leading to low drug accumulation at the target site or its low phototoxicity.[13]

An attractive approach to overcome the above disadvantages is the use of nanocarriers for Hyp delivery. As previously shown, encapsulation of Hyp in a drug delivery system based on polyvinylpyrrolidone, poly(ethylene glycol), poly(lactic-*co*-

[a]*Institute of Macromolecular Chemistry, Czech Academy of Sciences, Heyrovského nám. 2, 162 00 Prague, Czech Republic. E-mail: horak@imc.cas.cz*
[b]*Center for Interdisciplinary Biosciences, Technology and Innovation Park, P.J. Šafárik University in Košice, Jesenná 5, 041 54 Košice, Slovakia. E-mail: veronika.huntosova@upjs.sk*
[c]*Institute of Animal Biochemistry and Genetics, Centre of Biosciences, Slovak Academy of Sciences, Dúbravská cesta 9, 840 05 Bratislava, Slovakia*
[d]*Department of Biophysics, Institute of Physics, Faculty of Science, P.J. Šafárik University in Košice, Jesenná 5, 041 54 Košice, Slovakia*
[e]*Institute of Experimental Physics, Slovak Academy of Sciences, Department of Biophysics, Watsonova 47, 040 01 Košice, Slovakia*

† Electronic supplementary information (ESI) available. See DOI: https://doi.org/10.1039/d4nr05348f

glycolic acid), or magnetic nanoparticles significantly improved drug accumulation in cells and its phototoxicity.[13,16] However, the development of novel Hyp-based drug delivery systems that are capable of simultaneously releasing the drug and visualizing the target area has the potential to significantly enhance the efficacy of PDT. This includes optimization of therapy parameters, treatment duration, dynamics of drug accumulation depending on carrier signal intensity, and identification of metastases by distinguishing normal healthy tissue from the malignant one.[9] Such systems can open new opportunities for personalized medicine. A very promising approach to combine PDT induced by Hyp delivery and bioimaging is the use of upconversion nanoparticles (UCNPs) excited in the near-infrared (NIR) region. UCNPs represent a new generation of luminophores with excellent optical properties such as low excitation rate, high photostability, lack of intermittent emission ("blinking") during continuous excitation, and no effect of particle size on the position of the emission peak.[17] Other advantages of NIR light include minimized photodamage to healthy biological tissue, the ability to excite at wavelengths that penetrate deep into the body, and a high signal-to-noise ratio with improved detection sensitivity due to the absence of autofluorescence from biomaterials.[18] Most UCNPs are based on a crystalline $NaYF_4$ host lattice with doped sensitizers such as Yb^{3+} or Nd^{3+} and emitters like Er^{3+} or Tm^{3+}. While Yb^{3+} allows the excitation of particles at 980 nm, the introduction of Nd^{3+} into lanthanide-based UCNPs shifts the absorption to 800 nm. Compared to the former excitation wavelength, the latter one has a higher ability to penetrate tissues, allowing for their deeper visualization while delivering Hyp for PDT. However, due to the large surface area of the nanoparticles that allows contact with different quenching molecules, the quantum efficiency of UCNPs is lower compared to bulk crystals. This problem can be overcome by introducing an additional shell on the particles, thus increasing the intensity of upconversion emission.[19] Another challenge is to ensure the biocompatibility and colloidal stability of UCNPs in aqueous media and to introduce functional groups for bioconjugation of target molecules. To tackle this, methods of particle hydrophilization such as ligand exchange,[20] oxidation,[21] coating with an inorganic shell (*e.g.* silica)[22] or encapsulation with an amphiphilic ligand have been proposed.[23]

In this work, $NaYF_4$:Yb^{3+},Er^{3+}@$NaYF_4$:Nd^{3+} core–shell upconversion nanoparticles (CS-UCNPs) were prepared and then endowed with biocompatibility and colloidal stability by coating with poly(*N*,*N*-dimethylacrylamide-*co*-2-aminoethyl acrylate)-alendronate [P(DMA-AEA)-Ale] obtained by a reversible addition–fragmentation chain transfer (RAFT) reaction. In the resulting CS-UCNP@P(DMA-AEA)-Ale particles, PDMA provided sufficient steric stability in water and facilitated cellular uptake, which enhanced the efficacy of PDT, whereas AEA containing amino groups enabled conjugation of the Hyp photosensitizer. The particles allowed multimodal intracellular detection by both luminescence and Raman microspectroscopy.

2. Experimental

2.1. Materials

Chemicals, such as YCl_3, $YbCl_3$, $ErCl_3{\cdot}6H_2O$, $NdCl_3$, NH_4F, oleic acid (OA), *N*,*N*-dimethylacrylamide (DMA), 4,4′-azobis(4-cyanovaleric acid) (ACVA), 2-(dodecylthiocarbonothioylthio)-2-methylpropionic acid (DMP; chain transfer agent – CTA, *N*,*N*′-dicyclohexylcarbodiimide (DCC), *N*-hydroxysuccinimide (NHS), 2,2′-azobis(2-methylpropionitrile) (AIBN), *N*,*N*-diisopropylethylamine (DIPEA; ≥99%), octadec-1-ene (OD), 1,3-diphenylisobenzofuran (DPBF), phosphate buffered saline (PBS; pH = 7.4), and Dulbecco's modified Eagle's medium (DMEM) were purchased from Sigma-Aldrich (St Louis, MO, USA). Artificial lysosomal fluid (ALF; pH = 4.5) was prepared according to the literature.[24] 2-Hydroxy-3-morpholinopropanesulfonic acid (MOPSO; ≥99%) was purchased from Fluka (Charlotte, NC, USA). Sodium salt of (4-amino-1-hydroxy-1-phosphonobutyl) phosphonic acid trihydrate (alendronate; Ale) was from TCI (Tokyo, Japan). Hypericin (Hyp; ESI; Fig. S1†) was purchased from Thermo Fisher Scientific (Heysham, UK). Ethanol for UV spectroscopy and absolute ethanol were purchased from Lachner (Neratovice, Czech Republic) and VWR (Radnor, PA, USA), respectively. Acetic acid (99.8%), anhydrous sodium acetate (99.5%), and dimethyl sulfoxide (DMSO; 99.96%) were from Lachner. *tert*-Butyl[2-(acryloylamino)ethyl]carbamate) (AEC-Boc) was prepared according to the earlier report.[25] Other chemicals were obtained from Lachema (Brno, Czech Republic). Ultrapure Q-water was ultrafiltered on a Milli-Q Gradient A10 system (Millipore, Molsheim, France).

2.2. Synthesis of polymer coating

Poly(*N*,*N*-dimethylacrylamide-*co*-2-aminoethyl acrylate)-alendronate [P(DMA-AEA)-Ale] coating was prepared in a four-step procedure by modification of an earlier approach.[26] First, RAFT copolymerization of DMA with AEC-Boc (9/1 mol/mol) was initiated by ACVA (0.045 mmol) in the presence of a DMP chain transfer agent (0.2 mmol); the reaction proceeded at 70 °C for 30 min under an Ar atmosphere. The resulting poly (*N*,*N*-dimethylacrylamide-*co*-*tert*-butyl[2-(acryloylamino)ethyl] carbamate) [P(DMA-AEC-Boc)] was purified by precipitation in hexane. Second, the terminal CTA groups of P(DMA-AEC-Boc) were removed by refluxing a methanolic solution of the copolymer with AIBN for 2 h. The structure of the copolymer was confirmed by ^{1}H NMR spectroscopy; according to the results, the molar ratio of DMA/AEC-Boc in the polymer was 9/1 (Fig. S2a†). The molar mass of the polymer was 11 kg mol^{-1} with M_w/M_n = 1.2 according to GPC. Third, carboxyl groups of the copolymer were reacted with the amino groups of Ale *via* DCC/NHS activation according to the previously described procedure.[26] The formed P(DMA-AEC-Boc)-Ale was dialyzed using cellulose tubing against water (MWCO = 3.5 kDa; Spectrum Laboratories; Rancho Dominguez, CA, USA) for 48 h and freeze-dried. Fourth, amino groups of P(DMA-AEC-Boc)-Ale were deprotected in 3 M methanolic HCl at room temperature (RT) for 2 h with stirring. The resulting P(DMA-AEA)-Ale was purified by gel filtration in methanol on a Sephadex LH-10 column; the methanol was then evaporated on

a vacuum rotary evaporator. The presence of phosphorus in the copolymer was confirmed by ^{31}P NMR spectroscopy (δ = 18.4 ppm; Fig. S3†); the cleavage of Boc-groups was proved by the disappearance of the "e" peak in the ^{1}H NMR spectrum (Fig. S2b†).

2.3. Synthesis of $NaYF_4$:Yb^{3+},Er^{3+}@$NaYF_4$:Nd^{3+} core–shell nanoparticles (CS-UCNPs)

The core $NaYF_4$:Yb^{3+},Er^{3+} nanoparticles (C-UCNPs) were synthesized by a thermal decomposition method. Briefly, Y, Yb and Er oleates were obtained by a reaction of YCl_3 (305 mg), $YbCl_3$ (112 mg) and $ErCl_3{\cdot}6H_2O$ (15 mg) with OA (12 ml) in OD (30 ml) at 180 °C for 30 min with magnetic stirring under an Ar atmosphere. After cooling to RT, 0.5 mM methanolic NaOH solution (7 ml) and NH_4F (296 mg) were added and the mixture was heated at 300 °C for 90 min with stirring under an Ar atmosphere. The resulting C-UCNPs (~300 mg) were washed four times with hexane (12 ml each) using centrifugation (3460 rcf).

Separately, Y and Nd oleates were prepared from YCl_3 (312 mg), $NdCl_3$ (100 mg) and OA (12 ml) in OD (30 ml) as described above. A dispersion of C-UCNPs (150 mg) in hexane (10 ml) along with 0.125 mM methanolic NaOH solution, NH_4F (74 mg), OA (3 ml), and OD (7.5 ml) was added to Y and Nd oleates (10 ml) and the mixture was heated at 300 °C for 90 min with stirring under an Ar atmosphere. The resulting CS-UCNPs were sequentially washed with hexane, hexane/ethanol, ethanol, ethanol/water, and water as described above.

2.4. Coating of CS-UCNPs with P(DMA-AEA)-Ale

A dispersion of CS-UCNPs (40 mg) in water (2.4 ml) was added dropwise to an aqueous solution of P(DMA-AEA)-Ale (40 mg; 3.2 ml) in a 10 ml glass vial under sonication (Ultrasonic Homogenizer UP200S Hielscher; 20% power). Sonication was continued for 1 min, the vial was sealed with a rubber septum and the mixture was stirred at 80 °C for 18 h. The resulting CS-UCNP@P(DMA-AEA)-Ale particles were washed twice with water (2 ml each) using centrifugation (13 170 rcf) for 30 min.

2.5. Dissolution of CS-UCNP@P(DMA-AEA)-Ale nanoparticles

Dispersions of neat CS-UCNPs and CS-UCNP@P(DMA-AEA)-Ale particles (1 mg ml^{-1}) in water, 0.01 M PBS (pH = 7.4), DMEM with 10% fetal bovine serum, and ALF were placed in 2 ml plastic vials sealed with rubber septa and incubated at 37 °C for the given time with shaking (300 rpm). Subsequently, the particle dispersions were centrifuged (14 130 rcf) for 35 min to separate UCNPs and the supernatants were filtered (MWCO = 30 kg mol^{-1}) to remove residual particles. The amount of released F^- ions, defined as the molar percentage of F^-(X_F) relative to the amount of fluorine in the CS-UNCPs, was measured using a combined fluoride electrode (Thermo Fisher Scientific; Waltham, MA, USA).

2.6. Binding of hypericin (Hyp) to CS-UCNP@P(DMA-AEA)-Ale nanoparticles

A dispersion of CS-UCNP@P(DMA-AEA)-Ale nanoparticles (30 mg) in water/ethanol solution (0.75 ml; 1/1 v/v) was placed in an Eppendorf tube, DIPEA (6 µl) was added and the mixture was shaken (900 rpm) at RT for 20 min. The particles were separated by centrifugation (14 100 rcf) for 20 min, washed twice with absolute ethanol (2 ml) and redispersed in it. Then, the dispersion of CS-UCNP@P(DMA-AEA)-Ale nanoparticles (15 mg) in ethanol (1 ml) was added dropwise to a solution of Hyp (0.85 mg) in ethanol (2 ml) under sonication (25% power) for 1 min and the mixture was stirred at RT for 42 h in the dark. The resulting CS-UCNP@P(DMA-AEA)-Ale-Hyp nanoparticles were separated by centrifugation (14 100 rcf) for 20 min, washed ten times with DMSO (4 ml each), once with 0.05 M acetate buffer (pH = 6.4; 2 ml), twice with water (2 ml), each time using centrifugation (14 100 rcf) for 20 min, and redispersed in water. The Hyp content in the nanoparticles dispersed in DMSO was determined by UV-vis spectrophotometry at 602 nm using a calibration curve.

2.7. Hypericin release from CS-UCNP@P(DMA-AEA)-Ale-Hyp nanoparticles

The release of Hyp from nanoparticles was carried out in 0.05 M acetate buffer (pH = 4.8) and 0.05 M MOPSO buffer (pH = 7.4). The nanoparticle dispersion (1.4 mg ml^{-1}) in the corresponding buffer was shaken (750 rpm) at RT for 24 h. At selected time intervals, the samples (0.5 ml) were collected, the nanoparticles were separated by centrifugation (15 600 rcf) for 30 min, washed with DMSO/ethanol mixture (0.8 ml; 3/5 v/v), centrifuged and redispersed in DMSO (0.6 ml). The amount of released Hyp determined by UV-vis spectrophotometry at 602 nm was calculated as a percentage of the absorbance decrease at the selected time point compared to the initial absorbance at the zero point.

2.8. Determination of reactive oxygen species (ROS)

Singlet oxygen ($^1O_2$) generation was determined spectrophotometrically using a DPBF probe according to a previously described procedure.[27] Briefly, nanoparticle dispersion (0.2 ml; 2 mg ml^{-1}) in 0.05 M acetate buffer (pH = 4.8) or 0.05 M MOPSO buffer (pH = 7.4) was mixed with 0.01 mM DPBF in ethanol/buffer (1/1 v/v) to a volume of 2 ml. The mixture was then transferred into a quartz cuvette, which was sealed and irradiated with a 980 nm laser (MDL-III-980-2W; 2.11 W cm^{-2}) in the dark for 2 h with time intervals of 10 min. The absorption of DPBF was monitored with a Specord 250 Plus UV-vis spectrophotometer in the wavelength range of 350–650 nm as a function of exposure time; the decrease in peak intensity at 413 nm corresponded to $^1O_2$ formation.

2.9. Characterization methods

The morphology of the particles (shape, size, particle size distribution) was evaluated using a Tecnai G2 Spirit transmission electron microscope (TEM; FEI; Brno, Czech Republic) equipped with an energy-dispersive X-ray (EDX) detector (Mahwah, NJ, USA). At least 300 particles were counted to determine the number-average diameter D_n and size distribution (dispersity $Đ$) using ImageJ software (National Institutes of Health; Bethesda, MD, USA). The hydrodynamic

diameter (D_h) and polydispersity (*PD*) of the particles were measured by dynamic light scattering (DLS) using a ZSU 5700 Zetasizer Ultra (Malvern Instruments; Malvern, UK). Photoluminescence spectra were measured on an FS5 spectrofluorometer (Edinburgh Instruments; Edinburgh, UK) equipped with a UV-vis Xe lamp and 808 and 980 nm CW lasers with 2 W output power (MDL-III-980). ^{1}H NMR and ^{31}P NMR spectra were acquired on a Bruker Avance III 600 spectrometer (Bruker; Billerica, MA, USA). Molar masses M_w, M_n and M_w/M_n of polymers were determined using a Shimadzu HPLC chromatograph (Tokyo, Japan) equipped with a UV-vis diode array and OptilabrEX refractive index and DAWN EOS multi-angle light scattering detectors (Wyatt; Santa Barbara, CA, USA). Infrared spectra were measured on a 100 T FTIR spectrometer (PerkinElmer; Waltham, MA, USA) using a Specac MKII Golden Gate single attenuated total reflection (ATR) instrument. Thermogravimetric analysis (TGA) was performed in air with a PerkinElmer TGA 7 analyzer (Norwalk, CT, USA) over a temperature range of 30–650 °C at a constant heating rate of 10 °C min^{-1}.

2.10. Cell culture

Jurkat cells (acute T-cell leukemia; ATCC; Manassas, VA, USA) were maintained under standard culture conditions as recommended by the supplier. Complete RPMI 1640 cell culture medium (LM-R1638/500; Biosera; Nuaille, France) was supplemented with 10% fetal bovine serum (FBS; Gibco-Invitrogen, Life Technologies; Paisley, UK) and 1% w/w penicillin/streptomycin (Gibco-Invitrogen). Cells were grown until confluence in the dark at 37 °C under a 5% CO_2 atmosphere. Prior to the experiment, cells were centrifuged (690 rcf) for 6 min and diluted to the desired concentration (10^4 cells per well in 96-well plates or 5×10^4 cells per ml for microscopy and flow cytometry). The manipulation of cells during the experiments was performed in the dark with minimal use of light.

2.11. Flow cytometry

Cells were collected and distributed into 2 ml Eppendorf tubes in 1 ml aliquots (5×10^4 cells). These aliquots were supplemented with nanoparticle dispersions at concentrations of 0.01 and 0.1 mg ml^{-1} and left in the dark at 37 °C and 4 °C for 1 h. After incubation, hypericin uptake by Jurkat cells was measured with a CytoFLEX S flow cytometer (Beckman Coulter; Brea, CA, USA) in the Y610 channel. At least 10^4 cells were collected for analysis.

For the apoptotic study, cells were treated with nanoparticles (0.1 mg ml^{-1}) and irradiated according to the protocol. Prior to measurement, cells were detached with trypsin/ethylenediaminetetraacetic acid solution, which stopped the activity of the complete culture medium. A total of 0.5 ml of cell suspension was incubated for 15 min with the NucView® 488 caspase-3 substrate (Biotium; Fremont, CA, USA) to evaluate the level of caspase-3 in the cells. A correlation plot of the two detection channels was generated from B525 (NucView® 488) and R660 (hypericin).

2.12. Confocal fluorescence microscopy

Cells (5×10^4) were seeded on a Petri dish with a coverslip for confocal fluorescence microscopy (SPL Life Sciences; Pocheon-si, Republic of Korea). The cells were incubated in the dark with 0.1 mg ml^{-1} CS-UCNP@P(DMA-AEA)-Ale or CS-UCNP@P(DMA-AEA)-Ale-Hyp particles and 1.08 μM Hyp at 37 °C for 1 and 3 h, respectively. Bright-field and fluorescence images were taken using an LSM700 inverted confocal fluorescence microscope (Zeiss; Oberkochen, Germany) with a 40× water-immersion objective and 555 nm laser excitation. Hyp emission was detected in the spectral region >580 nm. Cell lysosomes were stained with 200 nM LysoTracker™ Green (Thermo Fisher Scientific; Waltham, MA, USA) for 30 min (excitation 488 nm and emission 490–540 nm) and mitochondria were stained with 400 nM MitoTracker™ Orange CMTM/ROS (Thermo Fisher Scientific) for 30 min (excitation 555 nm and emission >580 nm). Image analysis was performed using ImageJ software version 1.54d.

Singlet Oxygen Sensor Green® (2 ng μl^{-1}; Thermo Fisher Scientific) was administered into Jurkat cells treated with CS-UCNP@P(DMA-AEA)-Ale-Hyp particles (0.096 mg ml^{-1}) for 24 h. Cells were incubated for 1 h in the dark or irradiated with 808 nm light by an infrared diode laser (Changchun New Industries Optoelectronics Technology; Changchun, China) at 1 W cm^{-2} for 1 h. Fluorescence images in the green (excitation 488 nm and emission 490–540 nm) and red (excitation 555 nm and emission >580 nm) channels were detected, analyzed using ImageJ software and the percentage of green-positive cells *versus* negative cell population was plotted.

Near-infrared images of nanoparticles in cells were detected with a Thorlabs camera (Newton, NJ, USA) after excitation with a 980 nm laser (Thorlabs) through a 100× Nikon PlanFluor NA 1.3 objective with oil immersion and SP 750 and BP 600–750 filters.

For multimodal imaging, the cell was entrapped in a microstructural chamber created by two-photon polymerization[28] of OrmoComp®, a biocompatible photoresist (Micro Resist Technology; Berlin, Germany).[29] The confocal image of OrmoComp® was detected using a 405 nm laser and emission < 490 nm. Cells were fixed with 4% paraformaldehyde for 7 min and washed three times with PBS before Raman microspectroscopy.

2.13. Raman microspectroscopy

Dispersive Raman spectra were obtained in the vis and NIR regions (Renishaw RL785 diode cw laser; λ_{exc} = 785 nm) using a Raman confocal microspectrometer (Renishaw inVia; Gloucestershire, UK) equipped with a Leica direct microscope, an electrically cooled CCD camera and a 1200 lines per mm diffraction grating. The NIR laser provides a significant reduction in autofluorescence and background absorbance, which are usually problematic when irradiating cells and tissues at visible or ultraviolet wavelengths. The system was calibrated and monitored prior to measurement using a Si wafer reference line (520.5 cm^{-1}) and a 20× objective. Spectra

were recorded in the wavelength range of 100–4000 cm^{-1} while working in a microclimate using a 100× microscope objective (NA = 0.9). The accumulation time for one spectrum was 10 s and three accumulations were collected for one measurement on each sample, with at least three independent measurements. Laser power per sample was ~2 mW. The reference spectra of fixed cells (control and particle-labeled) and particle dispersions were deposited on the Si–Au surface to suppress unwanted contributions from the glass substrate. The resulting spectra were averaged and the background was subtracted.

2.14. Cell toxicity

Cell toxicity was evaluated using the MTT assay (3-(4,5-dimethylthiazol-2-yl)-2,5-diphenyltetrazolium bromide; Sigma-Aldrich). Cells containing nanoparticles were exposed to photodynamic treatment (PDT) in the dark under 590 nm LED light at doses of 1–4 J cm^{-2}. Alternatively, light at a wavelength of 808 nm with an intensity of 1 W cm^{-2} was used for 1 h to stimulate the nanoparticles inside the cells. MTT assay was performed 5 and 24 h after PDT, which was applied 3 h after nanoparticle administration. Formazan absorption was detected using a SYNERGY HTX multi-mode reader (BioTek; Winooski, VT, USA) at 590 nm. Formazan crystals were observed by microscopy before dissolving them in DMSO.

2.15. Statistical analysis

Data were analyzed using Microsoft Excel and GraphPad Prism 9 software. Analysis of variance (two-way ANOVA) followed by Sidak's multiple comparison test or Tukey's *post hoc* test was used to compare groups. Tukey's *post hoc* test showed differences within irradiated and non-irradiated groups. Sidak's multiple comparison test showed differences between irradiated cells and cells incubated in the dark. The significance level was set as $p \leq 0.05$. Data are presented as mean ± SEM.

3. Results and discussion

3.1. Upconversion nanoparticles

$NaYF_4$:Yb^{3+},Er^{3+}@$NaYF_4$:Nd^{3+} core–shell nanoparticles (CS-UCNPs) were obtained by oleic acid-stabilized thermal decomposition of lanthanide precursors in OD. First, $NaYF_4$:Yb^{3+},Er^{3+} C-UCNPs were prepared, on which an active $NaYF_4$:Nd^{3+} shell was introduced in the second step to enhance the upconversion luminescence and prevent surface quenching. Since the UCNPs were prepared in an organic solvent (OD) and then washed with hexane, they were hydrophobic. However, it was necessary to transfer them to the aqueous phase to make them biocompatible (nontoxic) as required by biomedical applications, such as drug delivery, biosensing, biolabeling, *etc*. Replacement of the organic solvent (hexane) with water involved several purification steps with various ethanol/water mixtures to remove excess OA. The morphology investigated by TEM showed a typical spherical-like shape of C-UCNPs with a mean diameter D_n of 25 ± 2 nm and dispersity $Đ$ = 1.01 indicating almost monodisperse particle size distribution and demonstrating the good quality of the synthesized particles (Fig. 1a; Table 1). The shape of the CS-UCNPs changed from spherical to ellipsoidal due to the introduction of the anisotropic $NaYF_4$:Nd^{3+} shell. The ellipsoids were 31 ± 2 nm long and 26 ± 2 nm wide (Fig. 1b; Table 1). By comparing the micrographs, shell thickness was estimated to be ~3.5 nm. The TEM/EDX spectrum of CS-UCNPs confirmed the presence of Na, F, Y, Yb, Er, and Nd elements in the particles (Fig. 1e). The small peak of Er at ~6.9 keV was due to its low content. The C and Cu peaks in the spectrum originated from the supporting TEM grid. The hydrodynamic size of the C-UCNPs and CS-UCNPs in water measured by DLS confirmed the low polydispersity of the particles (*PD* ~0.15) as well as the fact that D_h was larger than D_n due to the presence of a solvated ionic layer around the particles and possible slight aggregation (Table 1). The D_h of CS-UCNPs was larger than that of C-UCNPs due to the presence of the $NaYF_4$:Nd^{3+} shell. The ζ-potential of both C- and CS-UCNPs was ~30 mV; its positive value was due to the cationic nature of the metal ions of the particles.

The upconversion luminescence of CS-UCNPs was characterized by emission under 980 and 808 nm excitation (Fig. 2a). The emission showed four characteristic peaks at 409 ($^2H_{9/2} \rightarrow {}^4I_{15/2}$), 525 ($^2H_{11/2} \rightarrow {}^2I_{15/2}$), 540 ($^4S_{3/2} \rightarrow {}^2I_{15/2}$), and 654 nm ($^4F_{9/2} \rightarrow {}^2I_{15/2}$) typical of the transitions of Er^{3+} ions in UCNPs (Fig. 2a and b). At the same particle concentration in water (1 mg ml^{-1}) and laser power (0.6 W) under 980 nm excitation, the emission peak intensities of CS-UCNPs at 540 nm and 650 nm increased 6 and 7 times, respectively, compared to C-UCNPs (Fig. S4†). The dual excitation wavelengths of 980 and 808 nm make these particles a promising candidate for the development of an imaging-guided Hyp delivery system. Excitation at 980 nm is suitable for monitoring particle accumulation in cells *in vitro* without autofluorescence, while the 808 nm wavelength can provide *in vivo* visualization without local overheating due to low water absorption at this wavelength. The ATR-FTIR spectrum of CS-UCNPs exhibited tiny bands at 2927, 2858, 1655, and 1557 cm^{-1} probably assigned to asymmetric $\nu_{as}(CH_2)$, symmetric $\nu_s(CH_3)$, $\nu(C{=}C)$, and asymmetric $\nu_{as}(COO^-)$ stretching vibrations, respectively (Fig. S5a†). This indicated the presence of oleic acid residues on the particle surface after washing.[30] According to TGA, the CS-UCNPs contained ~2% oleic acid (Fig. S5b†), leaving a large portion of the particle surface available for P(DMA-AEA)-Ale binding.

3.2. CS-UCNP@P(DMA-AEA)-Ale nanoparticles

To make the CS-UCNPs biocompatible and colloidally stable in aqueous media, they were coated with P(DMA-AEA)-Ale obtained by RAFT copolymerization (Fig. S6†). The advantage of alendronate is that its terminal bisphonate groups bind tightly by coordination with lanthanides on the surface of UCNPs, while the benefit of PDMA is that it is a highly hydrophilic nontoxic polymer that provides sufficient steric stability of the particles in water. In addition, the copolymer of DMA with AEA is a kind of cationic polymer that facilitates cellular uptake[31] and contains reactive amino groups capable of

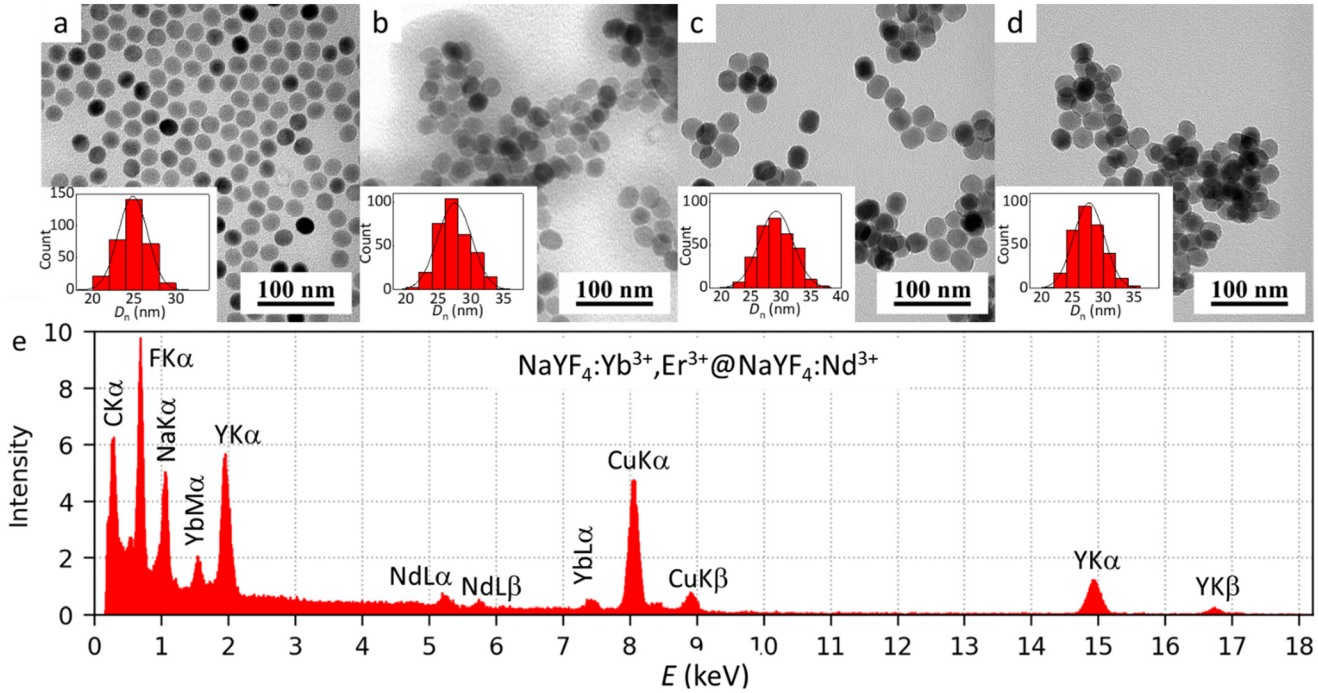

Fig. 1 TEM micrographs of (a) C-UCNPs, (b) CS-UCNPs, (c) CS-UCNP@P(DMA-AEA)-Ale, (d) CS-UCNP@P(DMA-AEA)-Ale-Hyp particles and (e) EDX of CS-UCNPs.

Table 1 Characterization of the particles[a]

	D_n (nm)	$Đ$	D_h (nm)	PD	ζ-Potential (mV)	Hyp content (mg g^{-1})
C-UCNPs	25	1.01	104 ± 1	0.15	30 ± 2	—
CS-UCNPs	31[c] (26[d])	1.01	158 ± 1	0.14	28 ± 3	—
CS-UCNP@P(DMA-AEA)-Ale	31[c] (27[d])	1.01	127 ± 2 (105 ± 2)[b]	0.10	20 ± 0.5	—
CS-UCNP@P(DMA-AEA)-Ale-Hyp	30[c] (25[d])	1.01	171 ± 6 (114 ± 1)[b]	0.26	18 ± 4	5.54

[a] C(CS)-UCNPs – core (core–shell) upconversion nanoparticles; P(DMA-AEA)-Ale-Hyp – poly(*N*,*N*-dimethylacrylamide-*co*-2-aminoethyl acrylate)-alendronate-hypericin; Hyp – hypericin; D_n – number-average diameter (TEM); $Đ$ – dispersity (TEM); D_h – hydrodynamic diameter in water; PD – polydispersity (DLS). [b] in DMEM. [c] Length. [d] Width.

binding Hyp. The D_n of CS-UCNP@P(DMA-AEA)-Ale particles was the same as that of CS-UCNPs (Fig. 1c), while the D_h of these particles in water (127 nm) was slightly lower than that of CS-UCNPs because the polymer coating stabilized the particles and reduced their aggregation (Table 1). In DMEM, the D_h of CS-UCNP@P(DMA-AEA)-Ale particles was lower (105 nm) than in water, which can be explained by the thinner ion solvation layer due to the presence of salts in the DMEM medium and thus lower aggregation. Also, the ζ-potential of CS-UCNP@P(DMA-AEA)-Ale nanoparticles (20 mV) was smaller than that of CS-UCNPs because Ale contains negatively charged phosphonate groups.

The upconversion luminescence spectra of CS-UCNP@P(DMA-AEA)-Ale particles obtained under 808 and 980 nm excitation had a similar intensity to those of CS-UCNPs (Fig. 2b and c). These results confirmed that the surface modification did not deteriorate the upconversion properties of the particles. In the FTIR spectrum of CS-UCNP@P(DMA-AEA)-Ale particles, a broad band at 3400 cm^{-1} corresponded to the ν(NH) and ν(OH) stretching vibrations of P(DMA-AEA)-Ale originating from the amine/amide moieties and water, respectively (Fig. S5a†). The asymmetric $\nu_{as}(CH_2)$ and ν(C=O) stretching vibrations were assigned to peaks at 2929 and 1630 cm^{-1}, respectively.[32] The TGA of CS-UCNP@P(DMA-AEA)-Ale particles showed that they contained 5.8 wt% of polymer coating (Fig. S5b†). Thus, both FTIR spectroscopy and TGA confirmed that the particle surface was successfully modified with P(DMA-AEA)-Ale.

3.3. Dispersion stability of CS-UCNP@P(DMA-AEA)-Ale nanoparticles

The dispersion stability of CS-UCNPs and CS-UCNP@P(DMA-AEA)-Ale nanoparticles in water, PBS, DMEM, and ALF was evaluated by DLS at 37 °C (Fig. 3a and b). In water, CS-UCNPs tended to aggregate as their hydrodynamic diameter increased after 7 days from ~160 nm to ~1400 nm. In contrast,

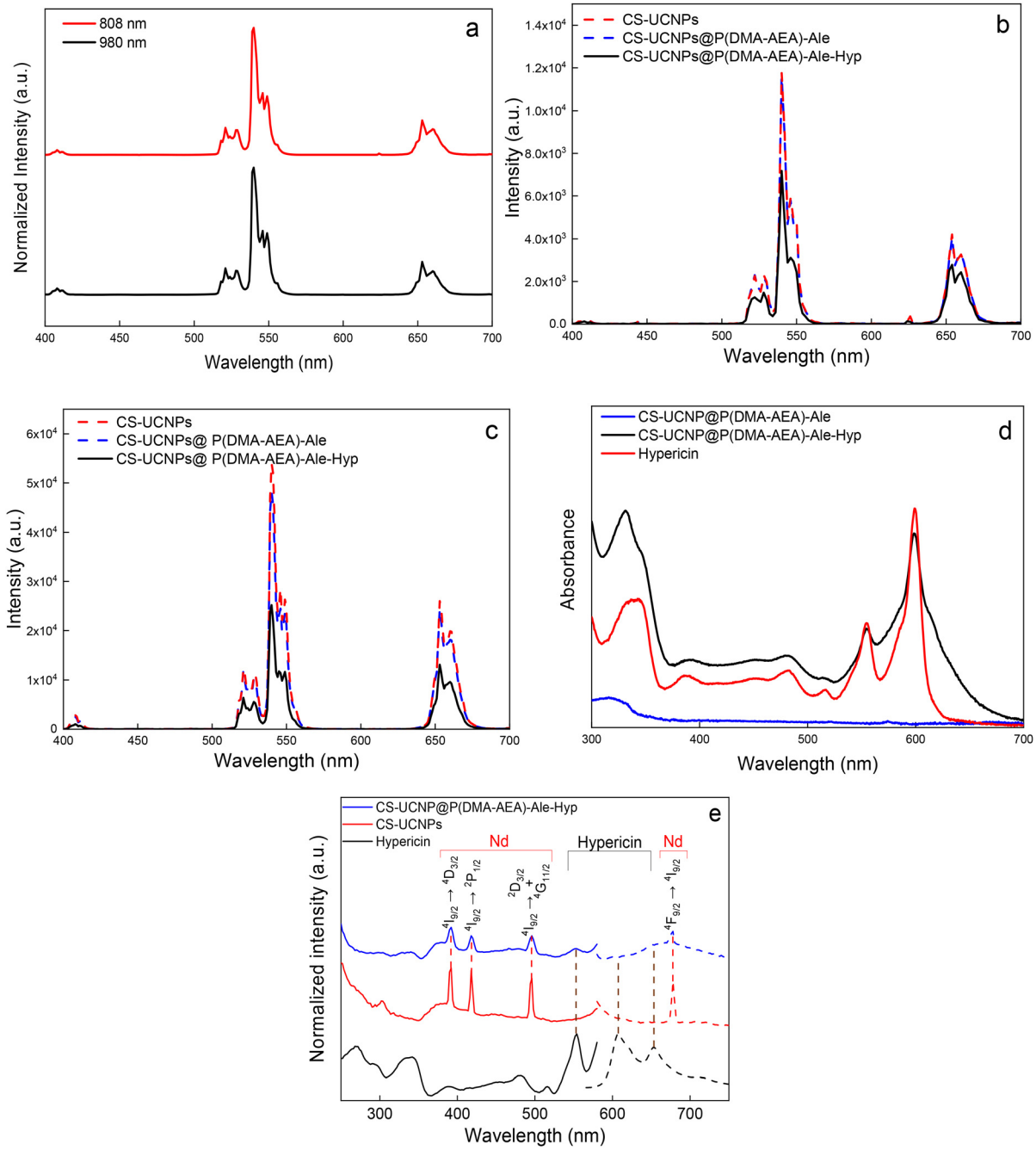

Fig. 2 (a) Upconversion luminescence spectra of CS-UCNPs in hexane under 808 and 980 nm excitation with a laser power of 2.11 W cm^{-2}. (b and c) Spectra of CS-UCNPs, CS-UCNP@P(DMA-AEA)-Ale and CS-UCNP@P(DMA-AEA)-Ale-Hyp nanoparticles in water excited at (b) 808 nm and (c) 980 nm. (d) UV-Vis absorption spectra of CS-UCNP@P(DMA-AEA)-Ale, CS-UCNP@P(DMA-AEA)-Ale-Hyp and hypericin. (e) Normalized photoluminescence excitation (solid line; λ_{em} = 607 nm) and emission spectra (dashed line; λ_{ex} = 554 nm) of hypericin, CS-UCNPs and CS-UCNP@P(DMA-AEA)-Ale-Hyp nanoparticles.

CS-UCNP@P(DMA-AEA)-Ale nanoparticles did not aggregate in water and were colloidally stable for 7 days. Both CS-UCNPs and CS-UCNP@P(DMA-AEA)-Ale particles were not stable in PBS because D_h increased rapidly to ~4500 nm and ~2200 nm, respectively, immediately after incubation due to interaction with phosphate ions. In DMEM, both CS-UCNPs and CS-UCNP@P(DMA-AEA)-Ale particles did not significantly aggregate for 3 days, but after 7 days, there was a slight increase in D_h for CS-UCNPs from ~300 nm to 460 nm. The D_h of CS-UCNPs and CS-UCNP@P(DMA-AEA)-Ale particles incubated in ALF increased similarly (~2500 nm), indicating that the polymer coating did not significantly affect the stability of the dispersion (Fig. 3a). Thus, the P(DMA-AEA)-Ale coating provided good stability to the CS-UCNPs in water and DMEM for

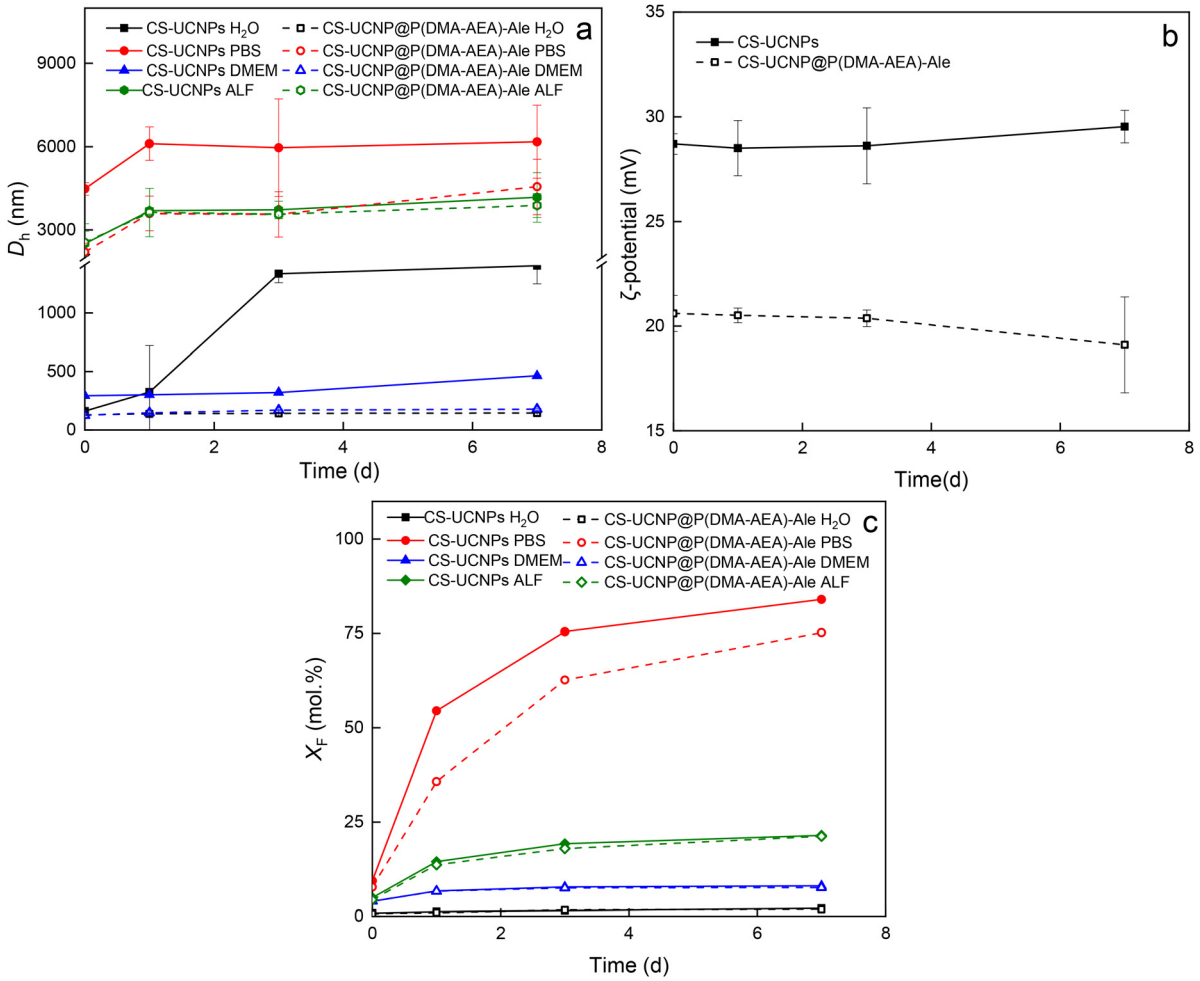

Fig. 3 Time dependence of (a) hydrodynamic diameter D_h, (b) ζ-potential and (c) F^- ion mole fraction (X_F) of CS-UCNPs and CS-UCNP@P(DMA-AEA)-Ale particles in supernatants after incubation of particles in water, PBS (pH = 7.4), DMEM and ALF at 37 °C.

at least 7 days, while the particles aggregated in PBS and ALF. The ζ-potential of CS-UCNPs and CS-UCNP@P(DMA-AEA)-Ale particles in water did not change significantly during 3 days (Fig. 3b). After 7 days, the ζ-potential of CS-UCNPs increased slightly due to partial dissolution and release of Ln^{3+} ions into the medium.

3.4. Dissolution of CS-UCNP@P(DMA-AEA)-Ale nanoparticles

It is known from the literature that UCNPs tend to dissolve in aqueous media, which impairs their luminescence properties and increases toxicity.[32–35] The dissolution rate depends on many factors such as particle composition, type of medium, temperature, pH, *etc*. The particles dissolved and released relatively little F^- ions in water, while most dissolved in PBS due to the formation of stable Ln-phosphate complexes accelerating hydrolysis. Also, elevated temperature is known to accelerate the dissolution of UCNPs.[33] Therefore, the molar fraction of F^- ions (X_F) of CS-UCNPs and CS-UCNP@P(DMA-AEA)-Ale particles in selected media modeling the biological conditions such as water, PBS, DMEM, and ALF was determined at 37 °C (Fig. 3c). Compared to CS-UCNPs, the chemical stability of CS-UCNP@P(DMA-AEA)-Ale particles in water, DMEM and ALF after 7 days increased only slightly, while it increased more significantly in PBS. P(DMA-AEA)-Ale showed relatively good protection against dissolution of CS-UCNPs in all tested media. The dissolution rates in water, DMEM and ALF were similar and slightly lower in PBS than those of previously investigated 25 nm UCNP@Ale-PDMA particles.[32,36] This behavior can be explained by the larger size and thus lower surface-to-volume ratio of CS-UCNPs.

3.5. Modification of CS-UCNP@P(DMA-AEA)-Ale particles with hypericin (Hyp)

Hypericin is an aromatic polycyclic dione containing six hydroxyls (Fig. S1†), which provides good photosensitivity and the ability to generate singlet oxygen due to the existence of an electron conjugated system.[37] Its main disadvantage is high hydrophobicity, which makes it very poorly soluble in water, making its use in photodynamic therapy problematic.[38] However, due to the presence of aromatic hydroxyls, Hyp has acidic properties (pK_a ~4.5) and forms sodium or amine salts.[38] This property was exploited to conjugate Hyp to the

P(DMA-AEA)-Ale polymer coating of UCNPs containing primary amino groups.

The D_n of UCNP@P(DMA-AEA)-Ale-Hyp particles was similar to that of CS-UCNPs (Fig. 1d; Table 1), indicating that the modification did not damage particles. The D_h of CS-UCNP@P(DMA-AEA)-Ale-Hyp particles in water (171 nm) was ~40 nm larger than that of CS-UCNP@P(DMA-AEA)-Ale particles due to the conjugation of hydrophobic Hyp, which may have reduced the hydrophilicity of the particles and thus increased their hydrodynamic diameter. In this respect, DLS confirmed the binding of Hyp to the particles. The D_h of the CS-UCNP@P(DMA-AEA)-Ale-Hyp particles in DMEM was smaller than that in water, similar to that of the CS-UCNP@P(DMA-AEA)-Ale particles. Conjugation of Hyp to the CS-UCNP@P(DMA-AEA)-Ale nanoparticles did not significantly change the ζ-potential of the CS-UCNP@P(DMA-AEA)-Ale-Hyp particles, which was 18 mV.

In contrast to the CS-UCNP@P(DMA-AEA)-Ale nanoparticles, the peaks in the upconversion luminescence spectra of the CS-UCNP@P(DMA-AEA)-Ale-Hyp particles were of lower intensity under excitation at both 808 and 980 nm (Fig. 2b and c), probably due to absorption by conjugated Hyp and the inner filter effect.[39,40] This was confirmed by a decrease in the upconversion intensity of CS-UCNP@P(DMA-AEA)-Ale and CS-UCNP@P(DMA-AEA)-Ale-Hyp nanoparticles with increasing irradiation time under 808 and 980 nm excitation in both the green and red emission bands (Fig. S7†). A more pronounced intensity decrease was observed under 980 nm excitation for CS-UCNP@P(DMA-AEA)-Ale-Hyp particles in both the green and red emission bands. However, the green-to-red emission intensity ratio under both 808 and 980 nm excitation decreased by 30% after conjugation of Hyp with CS-UCNP@P(DMA-AEA)-Ale nanoparticles confirming energy transfer between particles and Hyp. The FTIR spectrum of CS-UCNP@P(DMA-AEA)-Ale-Hyp nanoparticles was similar to that of CS-UCNP@P(DMA-AEA)-Ale. However, a new peak appeared at 773 cm^{-1} that was most probably assigned to the $\nu(C–H_{Ar})$ vibration originating from Hyp (Fig. S5a†). The UV-vis spectrum of CS-UCNP@P(DMA-AEA)-Ale-Hyp was also similar to that of neat Hyp (Fig. 2d), exhibiting two corresponding bands at 554 and 599 nm. According to UV-vis spectroscopy, the amount of Hyp in CS-UCNP@P(DMA-AEA)-Ale-Hyp particles was 5.54 mg g^{-1}. Therefore, both FTIR and UV-vis spectroscopy confirmed the presence of Hyp in the CS-UCNP@P(DMA-AEA)-Ale-Hyp particles. To further confirm the Hyp conjugation, photoluminescence excitation (λ_{em} = 607 nm) and emission (λ_{ex} = 554 nm) spectra of CS-UCNP@P(DMA-AEA)-Ale-Hyp nanoparticles were measured (Fig. 2e). The excitation peaks in the range from 250 to 500 nm were attributed to the $^4I_{9/2} \rightarrow {}^4D_{3/2}$ (391 nm), $^4I_{9/2} \rightarrow {}^2P_{1/2}$ (418 nm) and $^4I_{9/2} \rightarrow {}^2D_{3/2} + {}^4G_{11/2}$ (496 nm) transitions of Nd^{3+} emission.[41] Upon conjugation of Hyp with CS-UCNP@P(DMA-AEA)-Ale particles, an excitation peak at 554 nm appeared, whereas the CS-UCNP@P(DMA-AEA)-Ale particles alone did not show any characteristic photoluminescence peaks of Hyp. While free Hyp in DMSO showed typical intense peaks with emission maxima at 607 and 653 nm, the CS-UCNP@P(DMA-AEA)-Ale-Hyp nanoparticles exhibited Nd^{3+} emission at 680 nm ($^4F_{9/2} \rightarrow {}^4I_{9/2}$) and negligible Hyp emission at 607 nm. The characteristic Hyp emission band at 607 nm disappeared after its conjugation with the polymer-coated particles. This indicated that the bound Hyp lost its luminosity due to salt formation with amino groups, which is in agreement with the literature.[38] Nevertheless, the above results demonstrated that Hyp was successfully bound to the polymer coating of the nanoparticles.

3.6. Hypericin release from CS-UCNP@P(DMA-AEA)-Ale-Hyp nanoparticles and singlet oxygen generation

To ensure the efficacy of PDT for tumor cells, free Hyp released from the CS-UCNP@P(DMA-AEA)-Ale transport vehicle should be available in them. The release of Hyp was investigated at pH = 7.4 and 4.8 representing the physiological and cancer conditions, respectively (Fig. S8a†). Hyp release was four times higher in the acidic than in the physiological environment; within the first three hours of incubation, 44% of Hyp was released, compared to 11% in the slightly alkaline medium. After 24 h, 69% and 48% of Hyp was released from the particles at pH = 4.8 and 7.4, respectively. This difference can be explained by the protonation of the amino groups in PDMA at pH = 4.8, which led to swelling of the polymer coating due to repulsion between positively charged chains. This assumption was in agreement with earlier studies on drug delivery systems.[42,43] Such behavior of CS-UCNP@P(DMA-AEA)-Ale-Hyp nanoparticles will facilitate drug release in the acidic microenvironment of cancer and maintain its concentration in the tumor tissue, which may improve the effectiveness of PDT.

In addition, it was interesting to investigate the possibility of NIR-triggered PDT by the UCNP@P(DMA-AEA)-Ale nanoparticles, because UCNPs emit light at 542 nm and Hyp has one of the absorption bands at 554 nm, which can potentially lead to energy transfer and ROS formation. Singlet oxygen generation in the presence of CS-UCNP@P(DMA-AEA)-Ale-Hyp nanoparticles was determined using a DPBF probe at different pH values after irradiation with a 980 nm NIR laser. Exposure of a DPBF solution containing CS-UCNP@P(DMA-AEA)-Ale-Hyp particles to NIR light for 120 min caused a decrease in the absorption peak of DPBF at 415 nm in both acidic and slightly alkaline media, resulting in 13% and 10% degradation of DPBF, respectively (Fig. S8b–d†). Compared to free Hyp, Hyp conjugated to the particles showed no fluorescence, which would be associated with less effective singlet oxygen generation.[44,45] This could explain the lower photobleaching of DPBF under pH = 7.4, where the amount of released Hyp was smaller. To prove this assumption, a model experiment was performed, which confirmed significantly higher $^1O_2$ production by free Hyp compared to its conjugated form (Fig. S9†). Moreover, in the absence of particles, there was almost no degradation of DPBF during irradiation (Fig. S8d†). This suggests that the photobleaching of DPBF was primarily caused by ROS generation induced by energy transfer from CS-UCNPs to Hyp.

3.7. Distribution and uptake of CS-UCNP@P(DMA-AEA)-Ale-Hyp nanoparticles by Jurkat cells

Jurkat cells were chosen in this study as a model of cancer cells and for ease of their handling. The uptake of Hyp delivered to Jurkat cells by CS-UCNP@P(DMA-AEA)-Ale-Hyp particles was detected by confocal fluorescence microscopy (Fig. 4a) and flow cytometry (Fig. 4b). The distribution of CS-UCNP@P(DMA-AEA)-Ale-Hyp particles (0.1 mg ml^{-1}) and 1.08 μM Hyp in Jurkat cells after 3 h of incubation was very similar (Fig. 4a), although the concentration of Hyp in CS-UCNP@P(DMA-AEA)-Ale-Hyp was only 1.1 nM. Depending on their size, nanoparticles are thought to be preferentially taken up by cells *via* endocytosis, *i.e.* active transport.[46,47] To determine the rate of Hyp transport into cells, endocytosis was inhibited by incubating cells with CS-UCNP@P(DMA-AEA)-Ale-Hyp particles at 4 °C. Here, the fluorescence intensity of Hyp in the cells was significantly weaker than in cells incubated at 37 °C (Fig. 4b). Inhibition of endocytosis has previously been shown to reduce Hyp fluorescence and the uptake of fluorescently labeled lipoproteins and polymeric micelles by glioblastoma cells.[48,49] In the present study, Hyp fluorescence in the cells was reduced due to the inhibition by endocytosis. It can therefore be assumed that the uptake of UCNP@P(DMA-AEA)-

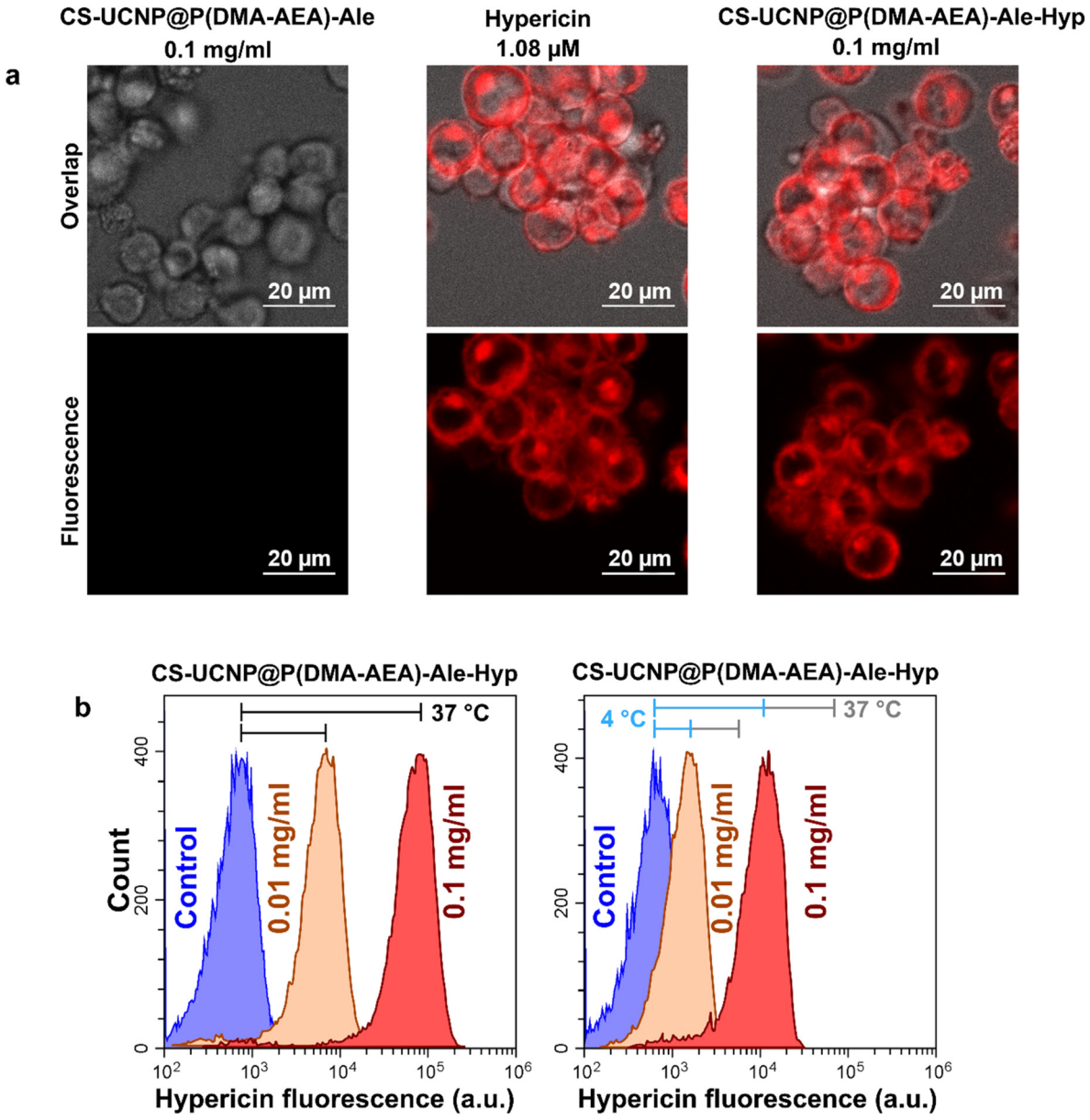

Fig. 4 (a) Fluorescence of Hyp (red) and overlap of the bright-field image with the fluorescence image of Jurkat cells incubated with 0.1 mg ml^{-1} CS-UCNP@P(DMA-AEA)-Ale, 1.08 μM Hyp and 0.1 mg ml^{-1} CS-UCNP@P(DMA-AEA)-Ale-Hyp particles for 3 h. (b) Uptake of CS-UCNP@P(DMA-AEA)-Ale-Hyp nanoparticles (0.01 mg ml^{-1} – orange; 0.1 mg ml^{-1} – red) by Jurkat cells after 1 h of incubation detected by flow cytometry at 37 °C and 4 °C. Changes show intensity markers: black for 37 °C and cyan for 4 °C.

Hyp particles by the cells was partly controlled by the active transport of nanoparticles, similar to what was previously observed for low-density lipoproteins.[50] Hyp forms non-fluorescent aggregates in its carriers.[48,51,52] Therefore, the distribution and localization of Hyp in the lipid compartment of cells closely define the photodynamic activity of this molecule.

3.8. Induction of apoptosis by photodynamic treatment of Jurkat cells with CS-UCNP@P(DMA-AEA)-Ale-Hyp nanoparticles

The main target of the photodynamic effect is the mitochondria, an organelle that controls oxidation-reduction reactions in cells.[53] Together with nanoparticle-loaded lysosomes, mitochondria can trigger the appropriate cellular response.[54,55] Thus, PDT can cause significant damage at the subcellular level. Therefore, in this report, lysosomes and mitochondria were examined by confocal fluorescence microscopy after labeling Jurkat cells with LysoTracker™ Green and MitoTracker™ Orange CMTM/ROS. While LysoTracker™ Green is sensitive to low pH in lysosomes, MitoTracker™ Orange CMTM/ROS is a fluorescent probe that responds to mitochondrial membrane potential and oxidative stress in cells.

Green lysosomal vesicles were observed in Jurkat cells in the dark in the absence and the presence of CS-UCNP@P(DMA-AEA)-Ale-Hyp nanoparticles (Fig. 5a). Although the DPBF experiment confirmed that CS-UCNP@P(DMA-AEA)-Ale-

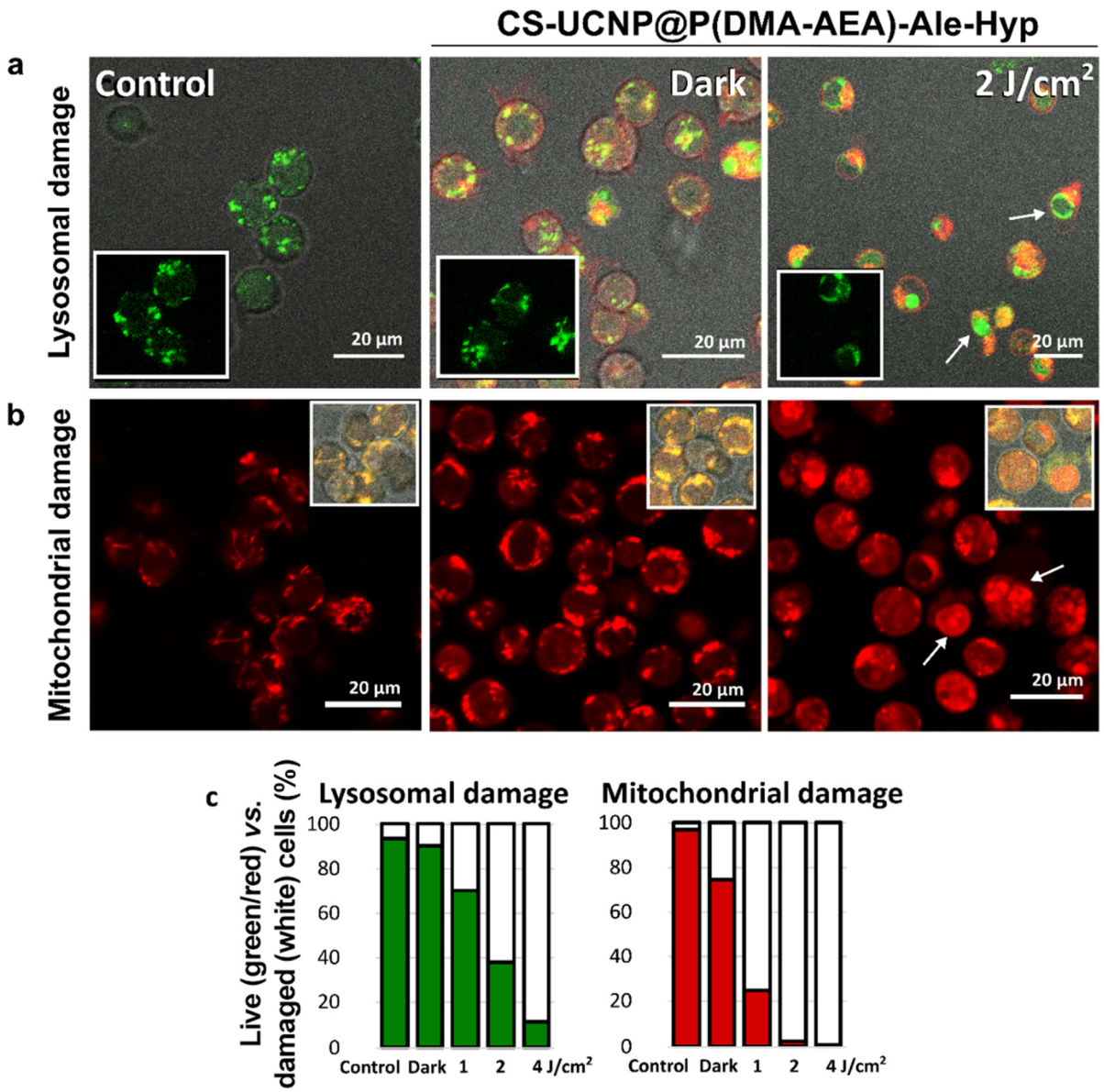

Fig. 5 Overlapping of representative fluorescence and bright-field images of Jurkat cells (a) labeled with LysoTracker™ Green (green; fluorescence images are in the insets); red fluorescence corresponds to Hyp. (b) The red fluorescence images correspond to MitoTracker™ Orange CMTM/ROS. The overlapping images are in the insets. Damaged cells are denoted with white arrows. (c) The histograms show percentage of damaged cells in lysosomes and mitochondria.

Hyp nanoparticles generated singlet oxygen after irradiation at 980 nm, our experimental design did not allow direct detection of changes in CS-UCNP@P(DMA-AEA)-Ale-Hyp-labeled Jurkat cells. This can be explained by the lower concentration of particles in the cells compared to that in the DPBF assay, which may lead to ROS formation at nontoxic concentrations, and increasing distance of the released Hyp from the particles reducing energy transfer and consequently ROS formation.[56] Nevertheless, CS-UCNP@P(DMA-AEA)-Ale nanoparticles remain an excellent delivery system and multimodal visualization agent. The efficiency of PDT mediated by Hyp transported into cells by nanoparticles was checked directly by the excitation of Hyp at 590 nm. Indeed, irradiation of these cells with this wavelength (2 J cm^{-2}) induced destruction of lysosomes, resulting in photodegradation of the fluorescent probe and its redistribution into the nuclei of damaged cells (denoted by white arrows in Fig. 5a). The number of cells with degraded lysosomal vesicles increased with increasing light dose (Fig. 5c). These results support the hypothesis that the CS-UCNP@P(DMA-AEA)-Ale-Hyp nanoparticles are taken by cells *via* endocytosis, as lysosomal vesicles were loaded with these particles, which after irradiation disrupted the organelles due to singlet oxygen generation.[57,58]

Autophagy is a type of cellular response, in which lysosomes are closely connected to mitochondria and their interplay is responsible for cell survival and demise.[59,60] Furthermore, mitochondria can generate and regulate oxidative stress. In the present study, MitoTracker™ Orange CMTM/ROS-labeled tubular structures associated with mitochondria were observed in Jurkat cells both in the absence and the presence of CS-UCNP@P(DMA-AEA)-Ale-Hyp particles (Fig. 5b). After oxidative stress has been developed, this fluorescent probe was degraded and relocalized to the nucleus, which was observed after irradiation (denoted with white arrows in Fig. 5b). The number of cells with labeled nuclei increased with the increasing light dose (Fig. 5c). This confirmed that the photodynamic reaction led to an increase in oxidative stress and induced specific cell signaling related to cell death.

With the aim to determine the type of cell death, the level of caspase-3 as an indicator of apoptosis was monitored in Jurkat cells. The ability to induce apoptosis by CS-UCNP@P(DMA-AEA)-Ale-Hyp nanoparticles after irradiation with 590 nm light was assessed by flow cytometry by measuring caspase-3 level with its substrate NucView® 488 Green. The cell population was divided into two parts: live cells that were

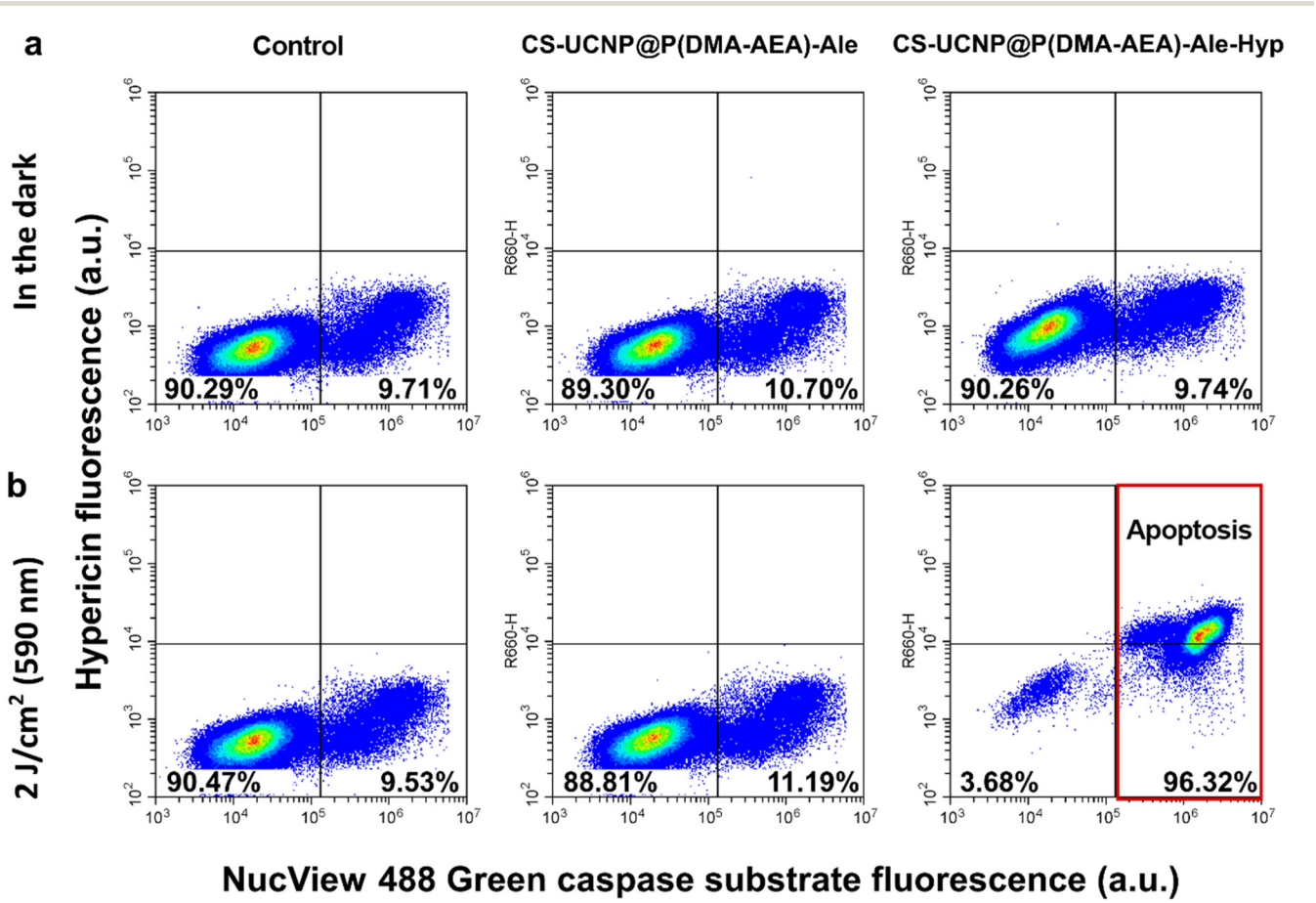

Fig. 6 Flow cytometry analysis of the caspase-3 level detected by NucView® 488 Green fluorescence in Jurkat cells incubated in the absence and the presence of 0.1 mg ml^{-1} CS-UCNP@P(DMA-AEA)-Ale and CS-UCNP@P(DMA-AEA)-Ale-Hyp (UCNP-Hyp) particles. Cells were analyzed after 24 h (a) in the dark and (b) after irradiation at 590 nm (2 J cm^{-2}). Correlation plots of Hyp and NucView® 488 fluorescence were color-coded from blue (minimum) to red (maximum). Cells that underwent apoptosis are denoted by the red rectangle in the right quadrants.

negative for caspase-3 (90%) and reference caspase-3 positive cells (~10%). No significant difference was observed between control cells and cells treated with CS-UCNP@P(DMA-AEA)-Ale nanoparticles after irradiation and in the dark (Fig. 6a and b). A similar effect was observed in cells treated in the dark with CS-UCNP@P(DMA-AEA)-Ale-Hyp particles (Fig. 6a). Irradiation of these cells significantly increased the number of caspase-3 positive cells (96%) and consequently the induction of apoptosis that is often observed by PDT mediated with Hyp.[61,62] Yang *et al.* observed that Hyp covalently bound to SiO_2 shell of UCNPs was able to increase caspase-3 levels and induce apoptosis in HeLa and HepG2 cells under NIR light irradiation.[63]

3.9. Efficacy of photodynamic treatment induced by CS-UCNP@P(DMA-AEA)-Ale-Hyp nanoparticles in Jurkat cells

To evaluate cell viability, the MTT test was used, which relies on the ability of viable cells to produce formazan upon the addition of the MTT reagent. In the context of PDT, cells containing Hyp either in solution[64,65] or bound to nanoparticles[66–68] exhibited significantly lower viability after PDT compared to the control.

In our results, the MTT assay, in contrast to Hyp (Fig. 7a), did not show a significant change in Jurkat cell viability when CS-UCNP@P(DMA-AEA)-Ale nanoparticles were added (Fig. 7b), *i.e.* their cytotoxic effect was absent. Although Tukey's *post hoc* test indicated a slight increase in viability with 0.05 mg ml^{-1} UCNP@P(DMA-AEA)-Ale particles after irradiation compared to the control ($p < 0.001$), this trend was not observed at other concentrations. In the case of CS-UCNP@P(DMA-AEA)-Ale-Hyp nanoparticles, formazan production was significantly reduced after irradiation compared to the control (two-way ANOVA; $p < 0.001$; Fig. 7c). Specifically, Tukey's *post hoc* test showed that cell viability significantly decreased after irradiation at Hyp concentrations of 0.55 nM and 1.1 nM in nanoparticles compared to the control ($p < 0.001$). Sidak's multiple comparison test confirmed that CS-UCNP@P(DMA-AEA)-Ale-Hyp nanoparticles significantly reduced formazan production only after 590 nm irradiation (2 J cm^{-2}), not in the dark.

It has been reported that the viability of cells treated with hypericin-based PDT decreased with increasing Hyp concentration in cancerous and non-cancerous cell lines.[69] When Hyp

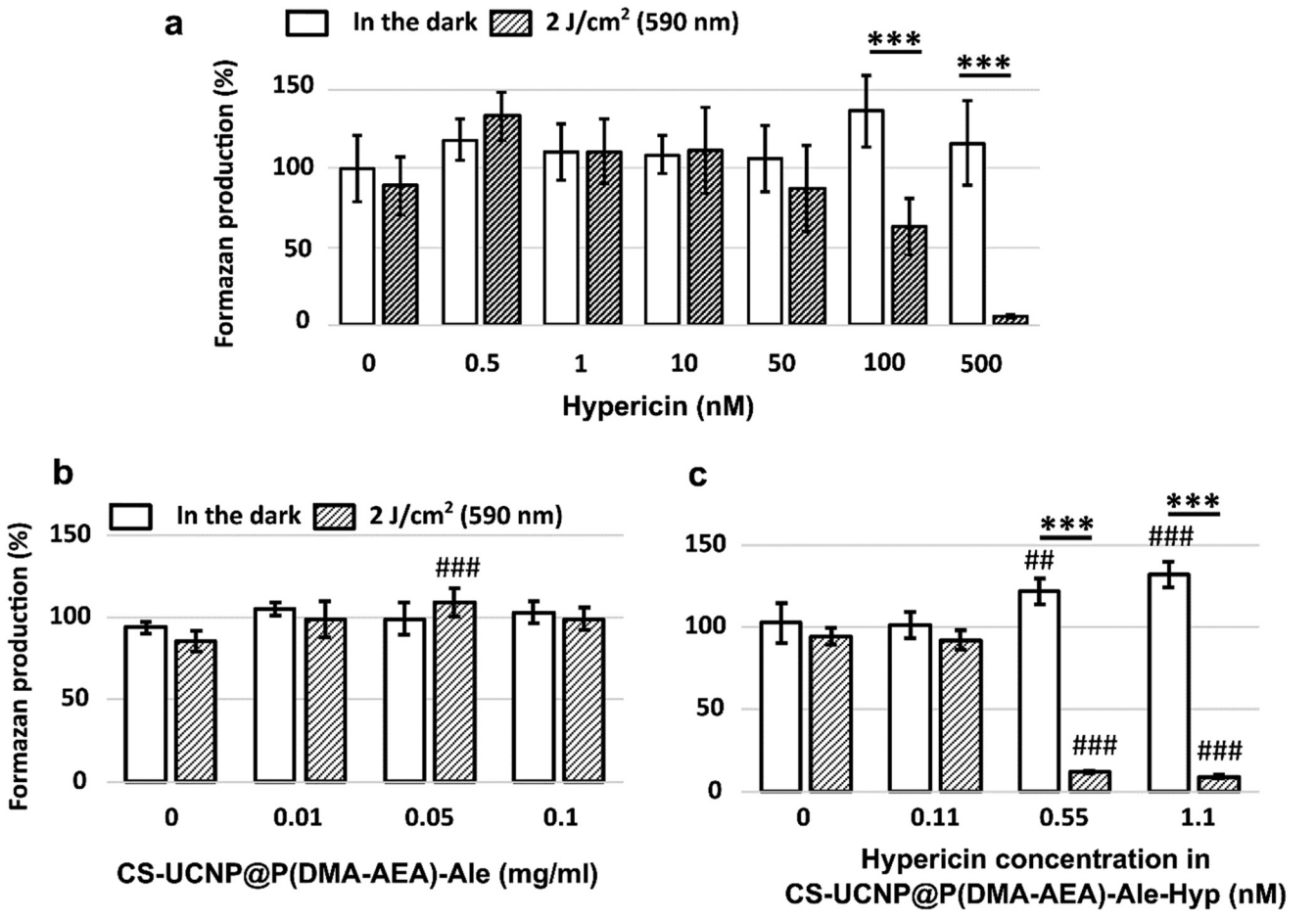

Fig. 7 MTT assay of Jurkat cells incubated with (a) Hyp, (b) CS-UCNP@P(DMA-AEA)-Ale and (c) CS-UCNP@P(DMA-AEA)-Ale-Hyp particles in the dark for 24 h (white bars) and for 3 h followed with irradiation at 590 nm and 2 J cm^{-2} (patterned bars). The level of significant differences was determined using a two-way ANOVA test. Tukey's *post hoc* test shows differences compared to the respective control, $^{\#\#}p < 0.01$, $^{\#\#\#}p < 0.001$. Sidak's multiple comparison test shows differences between irradiated and non-irradiated groups, $^{***}p < 0.001$.

was added directly to Jurkat cells, their viability decreased in a dose-dependent manner. Specifically, the application of 100 nM and 500 nM Hyp produced significantly less formazan compared to control (Sidak's multiple comparison test; $p < 0.001$; Fig. 7a). Hyp, whether alone or bound to CS-UCNP@P(DMA-AEA)-Ale particles, was cytotoxic. However, when Hyp was bound to particles, it proved to be more potent after irradiation and achieved significant cytotoxicity at much lower concentrations than Hyp alone.

The modification of the particles with Hyp allowed its internal stimulation with 808 nm light, although the efficiency of PDT was also weaker compared to irradiation with 590 nm light. This result correlates with the previously described PDT efficiency for CS-UCNP@P(DMA-AEA)-Ale-Hyp particles in the DPBF experiment and on Jurkat cells irradiated at 980 nm. Representative micrographs of formazan produced in Jurkat cells are shown in Fig. 8a. A significant reduction of formazan production in cells treated with 0.5 nM CS-UCNP@P(DMA-AEA)-Ale-Hyp particles was achieved by applying 1 W cm^{-2} for 1 h (Fig. 8b).

The ability to stimulate photodamage to Jurkat cells at 808 nm wavelength shortly after irradiation was assessed using Singlet Oxygen Sensor Green® (Fig. 8c). This agent can be located in damaged cells and its fluorescence increases upon singlet oxygen generation. A significantly higher number of damaged cells was found in the sample treated with CS-UCNP@P(DMA-AEA)-Ale-Hyp particles for 24 h and irradiated at 808 nm and 1 W cm^{-2} for 1 h (Fig. 8d). It should be noted that Jurkat cells are suspension cells, which reduces the efficiency of nanoparticle uptake. In contrast, adherent cell types are more amenable to uptake and therefore NIR-guided therapy will be more effective.

Although NIR-induced PDT was not highly effective for the cell line studied, both components of the developed CS-UCNP@P(DMA-AEA)-Ale system demonstrated their usefulness for improving PDT efficiency. While the nanoparticles allowed *in vitro* tracking of their accumulation in cells, the polymeric shell facilitated the uptake of the particles by the cells and increased the intracellular Hyp content.

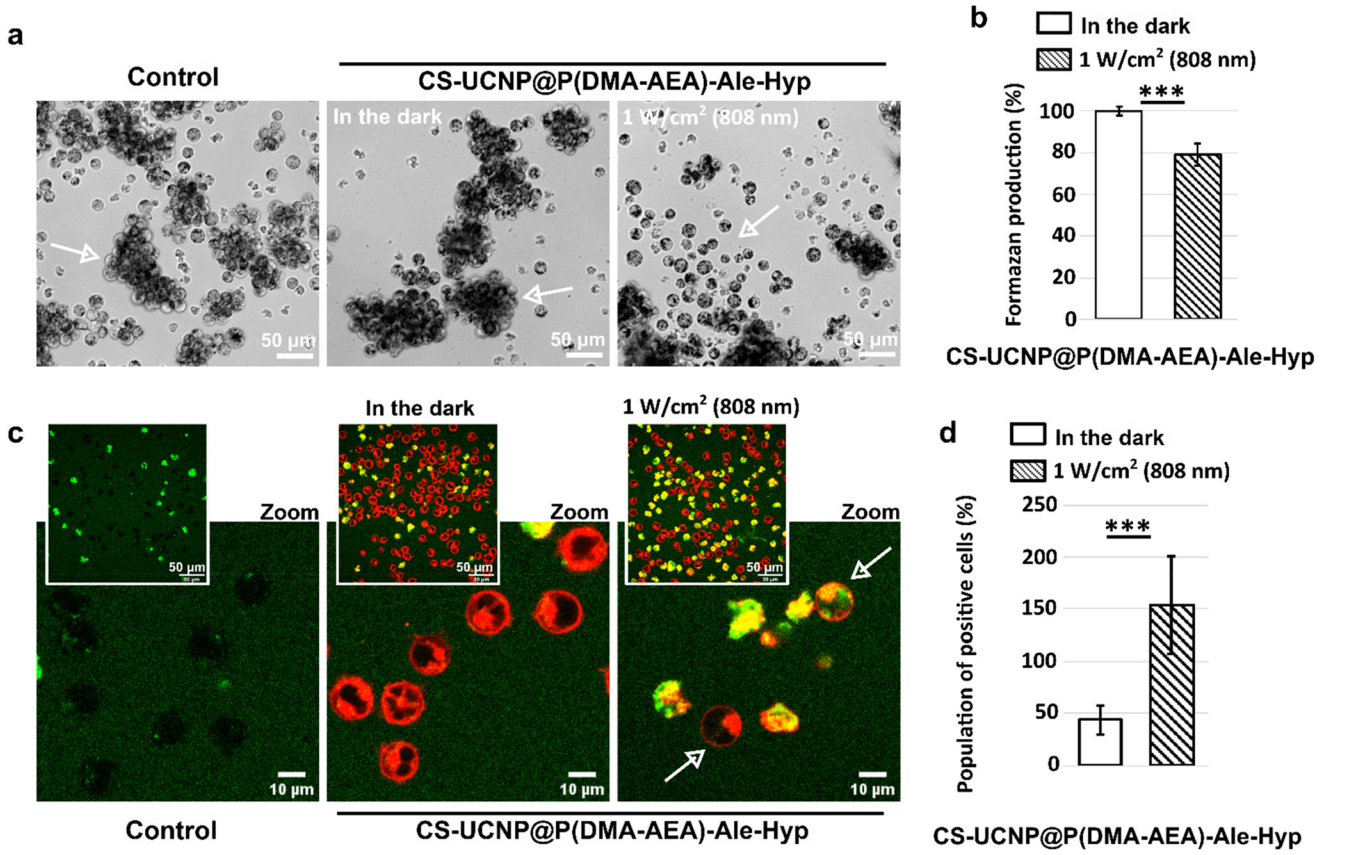

Fig. 8 (a) Bright-field images of Jurkat cells incubated with CS-UCNP@P(DMA-AEA)-Ale-Hyp particles for 24 h and irradiated at 808 nm and 1 W cm^{-2} for 1 h. The arrows show formazan crystals in a group of cells. (b) Formazan production was normalized to that obtained from cells incubated with particles in the dark and after irradiation. (c) Fluorescence images of Singlet Oxygen Sensor Green® (green) and hypericin (red) in cells treated with the particles for 1 h. Arrows show apoptotic cells damaged by the PDT effect (hypericin is mostly localized in the plasma membrane and not in the cytoplasm). (d) Population of Singlet Oxygen Sensor Green® positive cells treated with CS-UCNP@P(DMA-AEA)-Ale-Hyp particles for 24 h (white column) and irradiated for 1 h with 808 nm at 1 W cm^{-2} (patterned column). Statistical significance was determined by one-way ANOVA test: ***$p < 0.001$.

3.10. Multimodal imaging of CS-UCNP@P(DMA-AEA)-Ale-Hyp nanoparticles

Nanoparticles doped with lanthanides can be identified in cells using NIR imaging.[70] While no luminescence signal was detected in Jurkat cells without nanoparticles after stimulation with 980 nm laser light (Fig. 9a), bright red luminescent foci were detected in cells incubated with CS-UCNP@P(DMA-AEA)-Ale and CS-UCNP@P(DMA-AEA)-Ale-Hyp nanoparticles for 24 h (Fig. 9b and c). This luminescence was higher than Hyp fluorescence (Fig. 8d) and can be valuable for photodiagnosis of cancer cells prior PDT.[71]

Interestingly, the functionalization of CS-UCNP@P(DMA-AEA)-Ale nanoparticles with Hyp made them suitable for identification using Raman microspectroscopy. The Raman spectrum of control cells imaged in the "fingerprint region" (Fig. 9e) demonstrated molecular vibrations specific to chemical bonds, thus providing information about the biochemical composition of the sample, *i.e.* cellular constituents or building blocks such as proteins, nucleic acids, lipids, and carbohydrates.[72] Characteristic cellular vibrational bands were also clearly observed in the Raman spectrum of CS-UCNP@P(DMA-AEA)-Ale-Hyp-labeled Jurkat cells (Fig. 9f). However, the Raman signal of CS-UCNP@P(DMA-AEA)-Ale (Fig. 9g) significantly interfered with the cellular bands and defined the resulting spectrum.[73] In any case, the most intense band of particles at 1174 cm^{-1} proved to have great potential as a spectral marker for the search and detection of CS-UCNP@P(DMA-AEA)-Ale-labeled cells.

Finally, to verify the multimodal imaging of the designed nanoparticles, a Jurkat cell was entrapped in optical tweezers and transported to the microstructure chamber. The chamber was polymerized and used to localize cells in close proximity to study their interactions, such as responses to targeted treatments and their intercellular communication. While bright-field microscopy revealed CS-UCNP@P(DMA-AEA)-Ale-Hyp particles in the cell in red color, the confocal fluorescence image, *i.e.* OrmoComp® autofluorescence, was blue (Fig. 10a–d). The same sample was transferred into an NIR imaging setup and the luminescence of nanoparticles in the cell was imaged after excitation with 980 nm light (Fig. 10e and f). The detection pipeline was complemented by Raman microspectroscopy, which recorded the spectrum of CS-UCNP@P(DMA-AEA)-Ale-Hyp-labeled cells immobilized by formaldehyde fixation in an OrmoComp® microstructure chamber photopolymerized on a glass slide (Fig. 10g). Although a high number of intense bands related to OrmoComp® was found in the spectrum,[74] the Raman signal of cells and particles was also observed. The advantage of this multimodal imaging is in principle its simplicity and precision, especially when it comes to the possibility of using the same sample (one cell) in different imaging techniques without the need for further processing. This

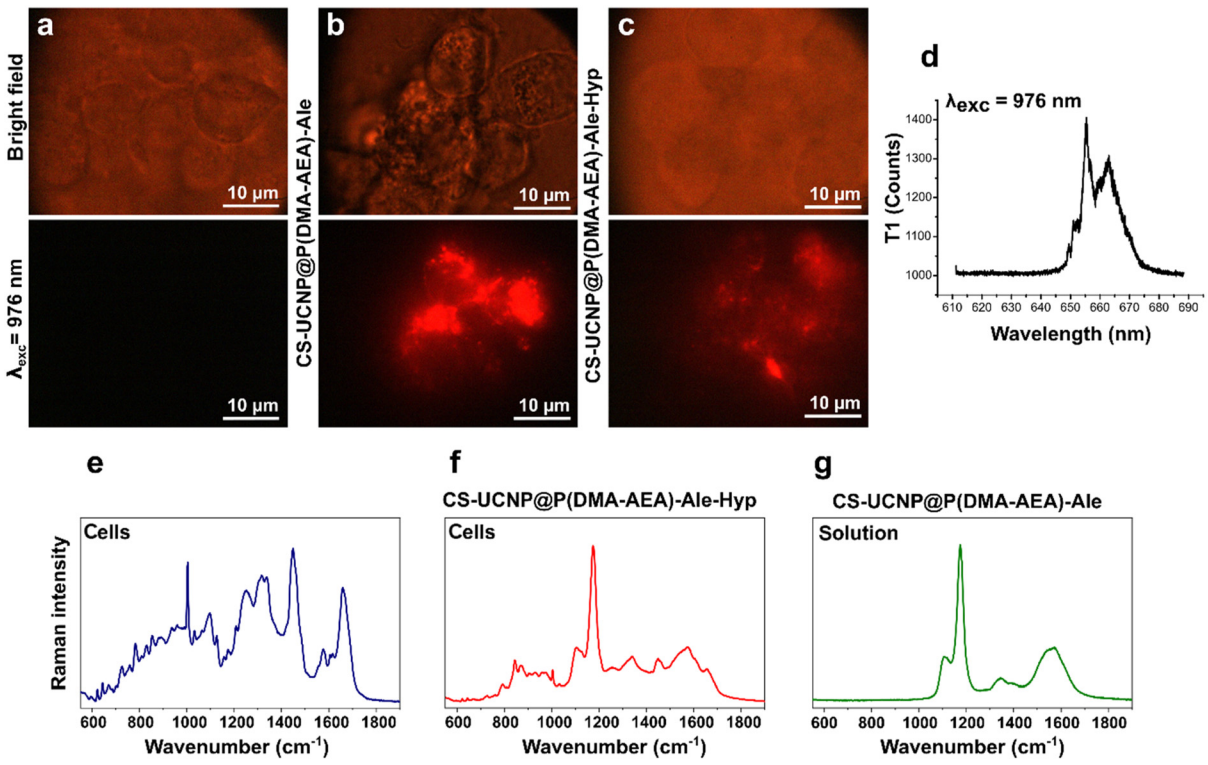

Fig. 9 Representative bright-field and luminescence images of (a) control Jurkat cells and cells incubated (b) with CS-UCNP@P(DMA-AEA)-Ale and (c) CS-UCNP@P(DMA-AEA)-Ale-Hyp particles for 24 h after excitation with 980 nm laser light. (d) Emission spectrum of CS-UCNP@P(DMA-AEA)-Ale-Hyp particles detected from solution after 980 nm laser excitation. (e) Raman spectrum of Jurkat cells and (f) cells labeled with CS-UCNP@P(DMA-AEA)-Ale-Hyp particles. (g) Raman spectrum of CS-UCNP@P(DMA-AEA)-Ale particles in aqueous solution.

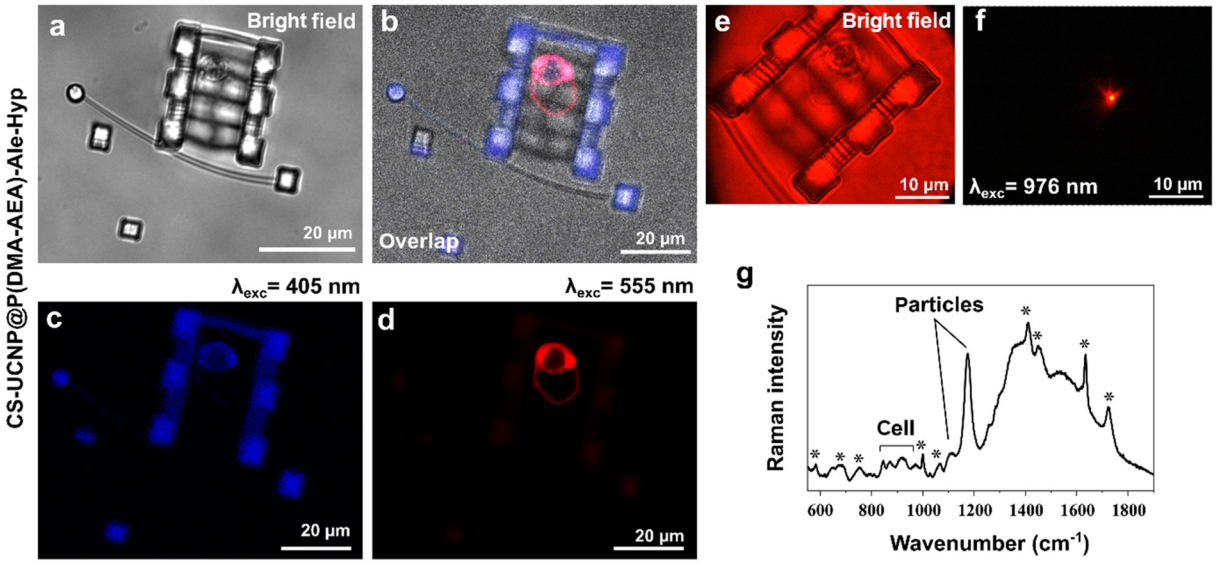

Fig. 10 (a) Representative bright-field and (b) fluorescence images of Jurkat cell entrapped in a microstructure chamber. (c) Autofluorescence of OrmoComp® microstructure (blue) and (d) Hyp fluorescence from CS-UCNP@P(DMA-AEA)-Ale-Hyp particles inside cell (red). (e) Bright-field image detected on NIR imaging setup and (f) the corresponding emission image after 980 nm excitation. (g) Raman spectrum detected from the position of a cell. Specific maxima for a cell, particles and OrmoComp® (*) are denoted.

allows more complete information to be obtained not only in terms of spectroscopy but also in terms of particle distribution in different tissues and cell morphology. In addition, cells in the microchamber can be immunolabelled and their response to treatment can be evaluated, or differences in Raman spectra corresponding to metabolic changes can be identified.

In general, multimodal imaging is important as a diagnostic tool for positive identification of cancer cells in histological samples from patient biopsies. Particles can be tuned according to the desired specificity towards cancer cells, *e.g.* by binding specific proteins with high affinity to cancer cell receptors. Thus, multimodal bioimaging of nanoparticles has good prospects for *in vivo* applications, including guided surgery and adjuvant photodynamic treatment.

4. Conclusions

Targeted drug delivery for the effective treatment of cancer remains a major challenge in contemporary medicine. To address this problem, we designed a novel advanced system based on CS-UCNPs to transport a highly powerful natural photosensitizer, hypericin, into tumor cells while monitoring their response to treatment. CS-UCNPs were prepared by thermal decomposition of rare earth oleates and coated with P(DMA-AEA)-Ale containing a phosphonate group with high affinity for particles. This coating enabled efficient transfer of the hydrophobic particles into the aqueous phase, ensuring their colloidal stability as well as biocompatibility. In addition, the reactive amino groups of P(DMA-AEA) allowed the binding of the Hyp photosensitizer for future PDT. Although the hydrophobicity of Hyp is a major drawback for its clinical use, UCNP@P(DMA-AEA)-Ale-Hyp nanoparticles represent a novel way to increase Hyp bioavailability to target tissues, including cancerous ones. Hyp release from CS-UCNP@P(DMA-AEA)-Ale-Hyp nanoparticles was significantly higher in the acidic environment of tumor cells than that at pH = 7.4, which is advantageous for efficient PDT of tumors. As a tumor tissue model, Jurkat cells were used, which readily engulfed the particles. At the same Hyp concentration, CS-UCNP@P(DMA-AEA)-Ale-Hyp particles were much more effective than pure Hyp for conventional PDT. Monitoring of caspase-3 then showed that apoptosis was responsible for the death of Jurkat cells containing CS-UCNP@P(DMA-AEA)-Ale-Hyp particles after irradiation at 590 nm. The cytotoxicity of the nanoparticles was also monitored by MTT assay, which showed that while the Hyp-free particles were not cytotoxic, the CS-UCNP@P(DMA-AEA)-Ale-Hyp particles induced a significant decrease in cell viability after irradiation. Finally, we highlighted the potential of the newly developed CS-UCNP@P(DMA-AEA)-Ale-Hyp nanoparticles not only as a suitable carrier for Hyp delivery to cancer cells, but also for multimodal tracking of cells using bright-field imaging, upconversion luminescence and Raman microspectroscopy. To the best of our knowledge, such a combination of specific imaging modalities for monitoring the targeting and fate of UCNPs in PDT of tumors is described for the first time.

Author contributions

TV – investigation, VH – conceptualization and formal analysis; VP – methodology; SO – visualization; CS – data curation; ZJ – investigation; GB – investigation; JK – data curation; MŠ –

visualization; OS – formal analysis; and DH – conceptualization and writing – original draft.

Data availability

The data supporting this article have been included as part of the ESI.†

Conflicts of interest

There are no conflicts of interest to declare.

Acknowledgements

Support of the Czech Science Foundation (No. 24-10125S) is acknowledged. VH thanks the Slovak Research and Development Agency through the projects APVV-20-0340 and APVV-21-0333, internal grant of Faculty of Science UPJS in Košice vvgs-2023-2556 and fellowships for excellent researchers R2–R4 project code: 09I03-03-V04-00007 as part of the Recovery and Resilience Plan for Slovakia.

References

1 L. Francés-Soriano, M. A. Zakharko, M. González-Béjar, P. A. Panchenko, V. Herranz-Pérez, D. A. Pritmov, M. A. Grin, A. F. Mironov, J. M. García-Verdugo, O. A. Fedorova and J. Pérez-Prieto, Nanohybrid for photodynamic therapy and fluorescence imaging tracking without therapy, *Chem. Mater.*, 2018, **30**, 3677–3682, DOI: 10.1021/acs.chemmater.8b00276.

2 Y. Jiang, Y. Hong, Y. Y. Liu, Y. Guan, J. Zhou, H. Wang and L. Sun, Switching between upconversion luminescence imaging and therapy *in vitro* enabled by NIR excitation modulation of nanocomposite, *J. Mater. Chem. C*, 2024, **12**, 11938–11947, DOI: 10.1039/D4TC01535E.

3 J. Zhou, M. Jiang, Q. Zhang, Y. Jiang, H. Wang and L. Sun, Alleviating hypoxia by integrating MnO_2 with metal-organic frameworks coated upconversion nanocomposites for enhanced photodynamic therapy *in vitro*, *Dalton Trans.*, 2025, **54**, 550–560, DOI: 10.1039/D4DT02605E.

4 A. E. O'Connor, W. M. Gallagher and A. T. Byrne, Porphyrin and nonporphyrin photosensitizers in oncology: Preclinical and clinical advances in photodynamic therapy, *Photochem. Photobiol.*, 2009, **85**, 1053–1074, DOI: 10.1111/j.1751-1097.2009.00585.x.

5 H. Wu, T. Minamide and T. Yano, Role of photodynamic therapy in the treatment of esophageal cancer, *Dig. Endosc.*, 2019, **31**, 508–516, DOI: 10.1111/den.13353.

6 S. Khan, M. A. B. Hussain, A. Khan, H. Liu, S. Siddiqui, S. Mallidi, P. Alacron, L. Daly, G. Rudd, F. Cuckov, C. Hopper, S. Bown, K. Akhtar, S. A. Hasan, S. A. Siddiqui, T. Hasan and J. P. Celli, Clinical evaluation of smartphone-based fluorescence imaging for guidance and monitoring of ALA-PDT treatment of early oral cancer, *J. Biomed. Opt.*, 2020, **25**, 063813, DOI: 10.1117/1.jbo.25.6.063813.

7 J. Usuda, T. Inoue, T. Tsuchida, K. Ohtani, S. Maehara, N. Ikeda, Y. Ohsaki, T. Sasaki and K. Oka, Clinical trial of photodynamic therapy for peripheral-type lung cancers using a new laser device in a pilot study, *Photodiagnosis Photodyn. Ther.*, 2020, **30**, 101698, DOI: 10.1016/j.pdpdt.2020.101698.

8 S. Anand, A. Yasinchak, T. Bullock, M. Govande and E. V. Maytin, A non-toxic approach for treatment of breast cancer and its metastases: Capecitabine enhanced photodynamic therapy in a murine breast tumor model, *J. Cancer Metastasis Treat.*, 2019, **5**, 6, DOI: 10.20517/2394-4722.2018.98.

9 J. F. Lovell, T. W. B. Liu, J. Chen and G. Zheng, Activatable photosensitizers for imaging and therapy, *Chem. Rev.*, 2010, **110**, 2839–2857, DOI: 10.1021/cr900236h.

10 P. Agostinis, K. Berg, K. A. Cengel, T. H. Foster, A. W. Girotti, S. O. Gollnick, S. M. Hahn, M. R. Hamblin, A. Juzeniene, D. Kessel, M. Korbelik, J. Moan, P. Mroz, D. Nowis, J. Piette, B. C. Wilson and J. Golab, Photodynamic therapy of cancer: An update, *Cancer J. Clin.*, 2011, **61**, 250–281, DOI: 10.3322/caac.20114.

11 T. E. Kim and J.-E. Chang, Recent studies in photodynamic therapy for cancer treatment: From basic research to clinical trials, *Pharmaceutics*, 2023, **15**, 2257, DOI: 10.3390/pharmaceutics15092257.

12 K. Liu, X. Liu, Q. Zeng, Y. Zhang, L. Tu, T. Liu, X. Kong, Y. Wang, F. Cao, S. A. G. Lambrechts, M. C. G. Aalders and H. Zhang, Covalently assembled NIR nanoplatform for simultaneous fluorescence imaging and photodynamic therapy of cancer cells, *ACS Nano*, 2012, **6**, 4054–4062, DOI: 10.1021/nn300436b.

13 G. P. de Andrade, T. F. M. de Souza, G. Cerchiaro, M. A. S. Pinhal, A. O. Ribeiro and M. J. B. C. Girão, Hypericin in photobiological assays: An overview, *Photodiagn. Photodyn.*, 2021, **35**, 102343, DOI: 10.1016/j.pdpdt.2021.102343.

14 L. Xu, X. Zhang, W. Cheng, Y. Wang, K. Yi, Z. Wang, Y. Zhang, L. Shao and T. Zhao, Hypericin-photodynamic therapy inhibits the growth of adult T-cell leukemia cells through induction of apoptosis and suppression of viral transcription, *Retrovirology*, 2019, **16**, 5, DOI: 10.1186/s12977-019-0467-0.

15 X. Yang, Q. Xiao, C. Niu, N. Jin, J. Ouyang, X. Xiao and D. He, Multifunctional core-shell upconversion nanoparticles for targeted tumor cells induced by near-infrared light, *J. Mater. Chem. B*, 2013, **1**, 2757–2763, DOI: 10.1039/c3tb00575e.

16 L. Mühleisen, M. Alev, H. Unterweger, D. Subatzus, M. Pöttler, R. P. Friedrich, C. Alexiou and C. Janko, Analysis of hypericin-mediated effects and implications for targeted photodynamic therapy, *Int. J. Mol. Sci.*, 2017, **18**, 1388, DOI: 10.3390/ijms18071388.

17 S. Wu, G. Han, D. J. Milliron, S. Aloni, V. Altoe, D. V. Talapin, B. E. Cohen and P. J. Schuck, Non-blinking

and photostable upconverted luminescence from single lanthanide-doped nanocrystals, *Proc. Natl. Acad. Sci. U. S. A.*, 2009, **106**, 10917–10921, DOI: 10.1073/pnas.0904792106.

18 S. Wilhelm, M. Kaiser, C. Würth, J. Heiland, C. Carrillo-Carrion, V. Muhr, O. S. Wolfbeis, W. J. Parak, U. Resch-Genger and T. Hirsch, Water dispersible upconverting nanoparticles: Effects of surface modification on their luminescence and colloidal stability, *Nanoscale*, 2015, **7**, 1403–1410, DOI: 10.1039/c4nr05954a.

19 X. Xu, Z. Zhou, Y. Liu, S. Wen, Z. Guo, L. Gao and F. Wang, Optimising passivation shell thickness of single upconversion nanoparticles using a time-resolved spectrometer, *APL Photonics*, 2019, **4**, 026104, DOI: 10.1063/1.5053608.

20 H. T. T. Duong, Y. Chen, S. A. Tawfik, S. Wen, M. Parviz, O. Shimoni and D. Jin, Systematic investigation of functional ligands for colloidal stable upconversion nanoparticles, *RSC Adv.*, 2018, **8**, 4842–4849, DOI: 10.1039/c7ra13765f.

21 H.-P. Zhou, C.-H. Xu, W. Sun and C.-H. Yan, Clean and flexible modification strategy for carboxyl/aldehyde-functionalized upconversion nanoparticles and their optical applications, *Adv. Funct. Mater.*, 2009, **19**, 3892–3900, DOI: 10.1002/adfm.200901458.

22 Q. Lü, F. Y. Guo, L. A. Sun, H. Li and L. C. Zhao, Silica-/titania-coated Y_2O_3:Tm^{3+}, Yb^{3+} nanoparticles with improvement in upconversion luminescence induced by different thickness shells, *J. Appl. Phys.*, 2008, **103**, 123533, DOI: 10.1063/1.2946730.

23 L.-L. Li, R. Zhang, L. Yin, K. Zheng, W. Qin, P. R. Selvin and Y. Lu, Biomimetic surface engineering of lanthanide-doped upconversion nanoparticles as versatile bioprobes, *Angew. Chem., Int. Ed.*, 2012, **51**, 6121–6125, DOI: 10.1002/anie.201109156.

24 C. Colombo, A. J. Monhemius and J. A. Plant, Platinum, palladium and rhodium release from vehicle exhaust catalysts and road dust exposed to simulated lung fluids, *Ecotoxicol. Environ. Saf.*, 2008, **71**, 722–730, DOI: 10.1016/j.ecoenv.2007.11.011.

25 T. Reschel, Č. Koňák, D. Oupický, L. W. Seymour and K. Ulbrich, Physical properties and *in vitro* transfection efficiency of gene delivery vectors based on complexes of DNA with synthetic polycations, *J. Controlled Release*, 2002, **81**, 201–217, DOI: 10.1016/S0168-3659(02)00045-7.

26 V. Oleksa, H. Macková, H. Engstová, V. Patsula, O. Shapoval, N. Velychkivska, P. Ježek and D. Horák, Poly(*N*,*N*-dimethylacrylamide)-coated upconverting $NaYF_4$:Yb, Er@$NaYF_4$:Nd core-shell nanoparticles for fluorescent labeling of carcinoma cells, *Sci. Rep.*, 2021, **11**, 21373, DOI: 10.1038/s41598-021-00845-y.

27 O. Shapoval, D. Větvička, V. Patsula, H. Engstová, O. Kočková, M. Konefał and D. Horák, Temoporfin-conjugated upconversion nanoparticles for NIR-induced photodynamic therapy: Studies with pancreatic adenocarcinoma cells *in vitro* and *in vivo*, *Pharmaceutics*, 2023, **15**, 2694, DOI: 10.3390/pharmaceutics15122694.

28 J. Kubacková, G. T. Iványi, V. Kažiková, A. Strejčková, A. Hovan, G. Žoldák, G. Vizsnyiczai, L. Kelemen, Z. Tomori and G. Bánó, Bending dynamics of viscoelastic photopolymer nanowires, *Appl. Phys. Lett.*, 2020, **117**, 013701, DOI: 10.1063/5.0014662.

29 C. Shizas and D. Karalekas, Mechanical characteristics of an Ormocomp® biocompatible hybrid photopolymer, *J. Mech. Behav. Biomed. Mater.*, 2011, **4**, 99–106, DOI: 10.1016/j.jmbbm.2010.09.010.

30 U. Kostiv, O. Janoušková, M. Šlouf, N. Kotov, H. Engstová, K. Smolková, P. Ježek and D. Horák, Silica-modified monodisperse hexagonal lanthanide nanocrystals: Synthesis and biological properties, *Nanoscale*, 2015, **7**, 18096–18104, DOI: 10.1039/C5NR05572E.

31 T. Näreoja, T. Deguchi, S. Christ, R. Peltomaa, N. Prabhakar, E. Fazeli, N. Perälä, J. M. Rosenholm, R. Arppe, T. Soukka and M. Schäferling, Ratiometric sensing and, imaging of intracellular pH using polyethylenimine-coated photon upconversion nanoprobes, *Anal. Chem.*, 2017, **89**, 1501–1508, DOI: 10.1021/acs.analchem.6b03223.

32 V. Patsula, D. Mareková, P. Jendelová, M. Nahorniak, O. Shapoval, P. Matouš, V. Oleksa, R. Konefał, M. Vosmanská, L. Machová-Urdziková and D. Horák, Polymer-coated hexagonal upconverting nanoparticles: Chemical stability and cytotoxicity, *Front. Chem.*, 2023, **11**, 1207984, DOI: 10.3389/fchem.2023.1207984.

33 D. Lisjak, O. Plohl, J. Vidmar, B. Majaron and M. Ponikvar-Svet, Dissolution mechanism of upconverting AYF_4:Yb,Tm (A = Na or K) nanoparticles in aqueous media, *Langmuir*, 2016, **32**, 8222–8229, DOI: 10.1021/acs.langmuir.6b02675.

34 E. Andresen, C. Würth, C. Prinz, M. Michaelis and U. Resch-Genger, Time-resolved luminescence spectroscopy for monitoring the stability and dissolution behavior of upconverting nanocrystals with different surface coatings, *Nanoscale*, 2020, **12**, 12589–12601, DOI: 10.1039/D0NR02931A.

35 N. Estebanez, M. González-Béjar and J. Pérez-Prieto, Polysulfonate cappings on upconversion nanoparticles prevent their disintegration in water and provide superior stability in a highly acidic medium, *ACS Omega*, 2019, **4**, 3012–3019, DOI: 10.1021/acsomega.8b03015.

36 M. Nahorniak, V. Patsula, D. Mareková, P. Matouš, O. Shapoval, V. Oleksa, M. Vosmanská, L. Machová Urdzíková, P. Jendelová, V. Herynek and D. Horák, Chemical and colloidal stability of polymer-coated $NaYF_4$:Yb,Er nanoparticles in aqueous media and viability of cells: The effect of a protective coating, *Int. J. Mol. Sci.*, 2023, **24**, 2724, DOI: 10.3390/ijms24032724.

37 J. Zhang, L. Gao, J. Hu, C. Wang, P. L. Hagedoorn, N. Li and X. Zhou, Hypericin: Source, determination, separation, and properties, *Sep. Purif. Rev.*, 2022, **51**, 1–10, DOI: 10.1080/15422119.2020.1797792.

38 L. Weiner and Y. Mazur, EPR study of hypericin-photogeneration of free-radicals and superoxide, *J. Chem. Soc., Perkin Trans.*, 1992, **2**, 1439–1442, DOI: 10.1039/p29920001439.

39 S. Chen, Y. L. Yu and J. H. Wang, Inner filter effect-based fluorescent sensing systems: A review, *Anal. Chim. Acta*, 2018, **999**, 13–26, DOI: 10.1016/j.aca.2017.10.026.

40 M. Zhao, H. Zhuang, B. Li, M. Chen and X. Chen, In situ transformable nanoplatforms with supramolecular cross-linking triggered complementary function for enhanced cancer photodynamic therapy, *Adv. Mater.*, 2023, **35**, e2209944, DOI: 10.1002/adma.202209944.

41 A. Bednarkiewicz, D. Wawrzynczyk, M. Nyk and W. Strek, Synthesis and spectral properties of colloidal Nd^{3+} doped $NaYF_4$ nanocrystals, *Opt. Mater.*, 2011, **33**, 1481, DOI: 10.1016/j.optmat.2011.01.006.

42 N. A. Nasab, H. H. Kumleh, M. Beygzadeh, S. Teimourian and M. Kazemzad, Delivery of curcumin by a pH-responsive chitosan mesoporous silica nanoparticles for cancer treatment, *Artif. Cells, Nanomed., Biotechnol.*, 2018, **46**, 75–81, DOI: 10.1080/21691401.2017.1290648.

43 F. R. Wibowo, O. A. Saputra, W. W. Lestari, M. Koketsu, R. R. Mukti and R. Martien, pH-Triggered drug release controlled by poly(styrene sulfonate) growth hollow mesoporous silica nanoparticles, *ACS Omega*, 2020, **5**, 4261–4269, DOI: 10.1021/acsomega.9b04167.

44 T. Yamazaki, N. Ohta, I. Yamazaki and P. S. Song, Excited-state properties of hypericin: Electronic spectra and fluorescence decay kinetics, *J. Phys. Chem.*, 1993, **97**, 7870–7875, DOI: 10.1021/j100132a013.

45 B. Rodríguez-Amigo, P. Delcanale, G. Rotger, J. Juárez-Jiménez, S. Abbruzzetti, A. Summer, M. Agut, F. J. Luque, S. Nonell and C. Viappiani, The complex of hypericin with β-lactoglobulin has antimicrobial activity with potential applications in dairy industry, *J. Dairy Sci.*, 2015, **98**, 89–94, DOI: 10.3168/jds.2014-8691.

46 R. Augustine, A. Hasan, R. Primavera, R. J. Wilson, A. S. Thakor and B. D. Kevadiya, Cellular uptake and retention of nanoparticles: Insights on particle properties and interaction with cellular components, *Mater. Today*, 2020, **25**, 101692, DOI: 10.1016/j.mtcomm.2020.101692.

47 J. Mosquera, I. García and L. M. Liz-Marzán, Cellular uptake of nanoparticles versus small molecules: A matter of size, *Acc. Chem. Res.*, 2018, **51**, 2305–2313, DOI: 10.1021/acs.accounts.8b00292.

48 V. Huntosova, D. Buzova, D. Petrovajova, P. Kasak, Z. Nadova, D. Jancura, F. Sureau and P. Miskovsky, Development of a new LDL-based transport system for hydrophobic/amphiphilic drug delivery to cancer cells, *Int. J. Pharm.*, 2012, **436**, 463–471, DOI: 10.1016/j.ijpharm.2012.07.005.

49 V. Huntošová, S. Datta, L. Lenkavská, M. Máčajová, B. Bilčík, B. Kundeková, I. Čavarga, J. Kronek, A. Jutková, P. Miškovský and D. Jancura, Alkyl chain length in poly(2-oxazoline)-based amphiphilic gradient copolymers regulates the delivery of hydrophobic molecules: A case of the biodistribution and the photodynamic activity of the photosensitizer hypericin, *Biomacromolecules*, 2021, **22**, 4199–4216, DOI: 10.1021/acs.biomac.1c00768.

50 V. Huntosova, L. Alvarez, L. Bryndzova, Z. Nadova, D. Jancura, L. Buriankova, S. Bonneau, D. Brault, P. Miskovsky and F. Sureau, Interaction dynamics of hypericin with low-density lipoproteins and U87-MG cells, *Int. J. Pharm.*, 2010, **389**, 32–40, DOI: 10.1016/j.ijpharm.2010.01.010.

51 V. Pevná, L. Zauška, A. Benziane, G. Vámosi, V. Girman, M. Miklóšová, B. Zeleňák, V. Huntošová and M. Almáši, Effective transport of aggregated hypericin encapsulated in SBA-15 nanoporous silica particles for photodynamic therapy of cancer cells, *J. Photochem. Photobiol., B*, 2023, **247**, 112785, DOI: 10.1016/j.jphotobiol.2023.112785.

52 A. M. Lima, C. D. Pizzol, F. B. Monteiro, T. B. Creczynski-Pasa, G. P. Andrade, A. O. Ribeiro and J. R. Perussi, Hypericin encapsulated in solid lipid nanoparticles: Phototoxicity and photodynamic efficiency, *J. Photochem. Photobiol., B*, 2013, **125**, 146–154, DOI: 10.1016/j.jphotobiol.2013.05.010.

53 D. E. Handy and J. Loscalzo, Redox regulation of mitochondrial function, *Antioxid. Redox Signaling*, 2012, **16**, 1323–1367, DOI: 10.1089/ars.2011.4123.

54 Y. Li, W. Han, D. Gong, T. Luo, Y. Fan, J. Mao, W. Qin and W. Lin, A self-assembled nanophotosensitizer targets lysosomes and induces lysosomal membrane permeabilization to enhance photodynamic therapy, *Chem. Sci.*, 2023, **14**, 5106–5115, DOI: 10.1039/D3SC00455D.

55 T. M. Tsubone, W. K. Martins, C. Pavani, H. Couto Junqueira, R. Itri and M. S. Baptista, Enhanced efficiency of cell death by lysosome-specific photodamage, *Sci. Rep.*, 2017, **7**, 6734, DOI: 10.1038/s41598-017-06788-7.

56 D. Steinebrunner, G. Schnurpfeil, M. Kohröde, A. Epp, K. Klangnog, J. A. T. Burgos, A. Wichmann, D. Wöhrle and A. Wittstock, Impact of photosensitizer orientation on the distance dependent photocatalytic activity in zinc phthalocyanine-nanoporous gold hybrid systems, *RSC Adv.*, 2020, **10**, 23203–23211, DOI: 10.1039/D0RA03891A.

57 B. Rodríguez-Amigo, P. Delcanale, G. Rotger, S. Juárez-Jiménez, A. Abbruzzetti, M. Summer, F. J. Agut, S. Luque, J. Nonell and C. Viappiani, The complex of hypericin with β-lactoglobulin has antimicrobial activity with potential applications in dairy industry, *J. Dairy Sci.*, 2015, **98**, 89–94, DOI: 10.3168/jds.2014-8691.

58 A. Hovan, V. Pevna, V. Huntosova, P. Miskovsky and G. Bánó, Singlet oxygen lifetime changes in dying glioblastoma cells, *Photochem. Photobiol.*, 2024, **100**, 159–171, DOI: 10.1111/php.13828.

59 M. Noguchi, N. Hirata, T. Tanaka, F. Suizu, H. Nakajima and J. A. Chiorini, Autophagy as a modulator of cell death machinery, *Cell Death Dis.*, 2020, **11**, 517, DOI: 10.1038/s41419-020-2724-5.

60 X. Ma, S. Manley, H. Qian, Y. Li, C. Zhang, K. Li, B. Ding, F. Guo, A. Chen, X. Zhang, M. Liu, M. Hao, B. Kugler, E. M. Morris, J. Thyfault, L. Yang, H. Sesaki, H. M. Ni, H. McBride and W. X. Ding, Mitochondria-lysosome-related organelles mediate mitochondrial clearance during cellular

dedifferentiation, *Cell Rep.*, 2023, **42**, 113291, DOI: 10.1016/j.celrep.2023.113291.

61 V. Pevná, M. Máčajová, A. Hovan, G. Bánó, M. Meta, B. Bilčík, J. Palková and V. Huntošová, Spheroidal model of SKBR3 and U87MG cancer cells for live imaging of caspase-3 during apoptosis induced by singlet oxygen in photodynamic therapy, *Biomedicines*, 2022, **10**, 2141, DOI: 10.3390/biomedicines10092141.

62 F. Guisier, P. Bohn, M. Patout, N. Piton, I. Farah, P. Vera, L. Thiberville and M. Salaün, *In-* and *ex vivo* molecular imaging of apoptosis to assess sensitivity of non-small cell lung cancer to EGFR inhibitors using probe-based confocal laser endomicroscopy, *PLoS One*, 2017, **12**, e0180576, DOI: 10.1371/journal.pone.0180576.

63 X. Yang, Q. Xiao, C. Niu, N. Jin, J. Ouyang, X. Xiao and D. He, Multifunctional core-shell upconversion nanoparticles for targeted tumor cells induced by near-infrared light, *J. Mater. Chem. B*, 2013, **1**, 2757–2763, DOI: 10.1039/c3tb00575e.

64 V. Pevna, D. Horvath, G. Wagnieres and V. Huntosova, Photobiomodulation and photodynamic therapy-induced switching of autophagy and apoptosis in human dermal fibroblasts, *J. Photochem. Photobiol., B*, 2022, **234**, 112539, DOI: 10.1016/j.jphotobiol.2022.112539.

65 M. Olek, A. Machorowska-Pieniążek, Z. P. Czuba, G. Cieślar and A. Kawczyk-Krupka, Effect of hypericin-mediated photodynamic therapy on the secretion of soluble TNF receptors by oral cancer cells, *Pharmaceutics*, 2023, **15**, 1279, DOI: 10.3390/pharmaceutics15041279.

66 D. Mokoena, B. P. George and H. Abrahamse, Conjugation of hypericin to gold nanoparticles for enhancement of photodynamic therapy in MCF-7 breast cancer cells, *Pharmaceutics*, 2022, **14**, 2212, DOI: 10.3390/pharmaceutics14102212.

67 H. Unterweger, D. Subatzus, R. Tietze, C. Janko, M. Poettler, A. Stiegelschmitt, M. Schuster, C. Maake, A. R. Boccaccini and C. Alexiou, Hypericin-bearing magnetic iron oxide nanoparticles for selective drug delivery in photodynamic therapy, *Int. J. Nanomed.*, 2015, **10**, 6985–6996, DOI: 10.2147/IJN.S92336.

68 M. Zeisser-Labouèbe, N. Lange, R. Gurny and F. Delie, Hypericin-loaded nanoparticles for the photodynamic treatment of ovarian cancer, *Int. J. Pharm.*, 2006, **326**, 174–181, DOI: 10.1016/j.ijpharm.2006.07.012.

69 M. Woźniak and M. Nowak-Perlak, Hypericin-based photodynamic therapy displays higher selectivity and phototoxicity towards melanoma and squamous cell cancer compared to normal keratinocytes *in vitro*, *Int. J. Mol. Sci.*, 2023, **24**, 16897, DOI: 10.3390/ijms242316897.

70 C. Arnau del Valle, T. Hirsch and M. J. Marín, Recent advances in near infrared upconverting nanomaterials for targeted photodynamic therapy of cancer, *Methods Appl. Fluoresc.*, 2022, **10**, 034003, DOI: 10.1088/2050-6120/ac6937.

71 A. Hovan, V. Pevna, V. Huntosova, P. Miskovsky and G. Bánó, Singlet oxygen lifetime changes in dying glioblastoma cells, *Photochem. Photobiol.*, 2024, **100**, 159–171, DOI: 10.1111/php.13828.

72 D. Steinebrunner, G. Schnurpfeil, M. Kohröde, A. Epp, K. Klangnog, J. A. T. Burgos, A. Wichmann, D. Wöhrle and A. Wittstock, Impact of photosensitizer orientation on the distance dependent photocatalytic activity in zinc phthalocyanine-nanoporous gold hybrid systems, *RSC Adv.*, 2020, **10**, 23203–23211, DOI: 10.1039/D0RA03891A.

73 S. Namagal, N. V. Jaya, M. Muralidharan and S. Sumithra, Optical and magnetic properties of pure and Er, Yb-doped β-$NaYF_4$ hexagonal plates for biomedical applications, *J. Mater. Sci.:Mater. Electron.*, 2020, **31**, 11398–11410, DOI: 10.1007/s10854-020-03689-w.

74 S. Fritzsche, B. R. Pauw, C. Weimann and H. Sturm, First of its kind: A test artifact for direct laser writing, *Meas. Sci. Technol.*, 2023, **34**, 075004, DOI: 10.1088/1361-6501/acc47a.